The Astrophysical Journal Supplement Series, 259:27 (24pp), 2022 March https://doi.org/10.3847/1538-4365/ac470b
© 2022. The Author(s). Published by the American Astronomical Society.
OPEN ACCESS

The Dark Energy Survey Bright Arcs Survey: Candidate Strongly Lensed Galaxy Systems from the Dark Energy Survey 5000 Square Degree Footprint

J. H. O'Donnell[1], R. D. Wilkinson[2], H. T. Diehl[3], C. Aros-Bunster[4], K. Bechtol[5], S. Birrer[6,7], E. J. Buckley-Geer[3,8], A. Carnero Rosell[9,10], M. Carrasco Kind[11,12], L. N. da Costa[9,10], S. J. Gonzalez Lozano[5], R. A. Gruendl[11,12], M. Hilton[13,14], H. Lin[3], K. A. Lindgren[3], J. Martin[15,16], A. Pieres[9,10], E. S. Rykoff[6,17], I. Sevilla-Noarbe[18], E. Sheldon[15], C. Sifón[4], D. L. Tucker[3], B. Yanny[3], T. M. C. Abbott[19], M. Aguena[9], S. Allam[3], F. Andrade-Oliveira[9,20], J. Annis[3], E. Bertin[21,22], D. Brooks[23], D. L. Burke[6,17], J. Carretero[24], M. Costanzi[25,26,27], J. De Vicente[18], S. Desai[28], J. P. Dietrich[29], K. Eckert[30], S. Everett[31], I. Ferrero[32], B. Flaugher[3], P. Fosalba[33,34], J. Frieman[3,35], J. García-Bellido[36], E. Gaztanaga[33,34], D. W. Gerdes[37,38], D. Gruen[29], J. Gschwend[9,10], M. S. S. Gill[6], G. Gutierrez[3], S. R. Hinton[39], D. L. Hollowood[31], K. Honscheid[40,41], D. J. James[42], T. Jeltema[31], K. Kuehn[43,44], O. Lahav[23], M. Lima[9,45], M. A. G. Maia[9,10], J. L. Marshall[46], P. Melchior[47], F. Menanteau[11,12], R. Miquel[24,48], R. Morgan[5], B. Nord[3,8,35], R. L. C. Ogando[10], F. Paz-Chinchón[12,49], M. E. S. Pereira[38,50], A. A. Plazas Malagón[47], M. Rodriguez-Monroy[18], A. K. Romer[2], A. Roodman[6,17], E. Sanchez[18], V. Scarpine[3], M. Schubnell[38], S. Serrano[33,34], M. Smith[51], E. Suchyta[52], M. E. C. Swanson[12], G. Tarle[38], D. Thomas[53], C. To[6,7,17], and T. N. Varga[54,55]

(DES Collaboration)

[1] Department of Physics, University of California at Santa Cruz, Santa Cruz, CA 95064, USA
[2] Department of Physics and Astronomy, Pevensey Building, University of Sussex, Brighton, BN1 9QH, UK
[3] Fermi National Accelerator Laboratory, P.O. Box 500, Batavia, IL 60510, USA; diehl@fnal.gov
[4] Instituto de Física, Pontificia Universidad Católica de Valparaíso, Casilla 4059, Valparaíso, Chile
[5] Physics Department, 2320 Chamberlin Hall, University of Wisconsin-Madison, 1150 University Avenue, Madison, WI 53706-1390, USA
[6] Kavli Institute for Particle Astrophysics & Cosmology, P.O. Box 2450, Stanford University, Stanford, CA 94305, USA
[7] Department of Physics, Stanford University, 382 Via Pueblo Mall, Stanford, CA 94305, USA
[8] Department of Astronomy and Astrophysics, University of Chicago, Chicago, IL 60637, USA
[9] Laboratório Interinstitucional de e-Astronomia—LIneA, Rua Gal. José Cristino 77, Rio de Janeiro, RJ—20921-400, Brazil
[10] Observatório Nacional, Rua Gal. José Cristino 77, Rio de Janeiro, RJ—20921-400, Brazil
[11] Department of Astronomy, University of Illinois at Urbana-Champaign, 1002 West Green Street, Urbana, IL 61801, USA
[12] Center for Astrophysical Surveys, National Center for Supercomputing Applications, 1205 West Clark Street, Urbana, IL 61801, USA
[13] Astrophysics Research Centre, University of KwaZulu-Natal, Westville Campus, Durban 4041, South Africa
[14] School of Mathematics, Statistics & Computer Science, University of KwaZulu-Natal, Westville Campus, Durban 4041, South Africa
[15] Brookhaven National Laboratory, Building 510, Upton, NY 11973, USA
[16] Half Hollow Hills High School East, 50 Vanderbilt Parkway, Dix Hills, NY 11746, USA
[17] SLAC National Accelerator Laboratory, Menlo Park, CA 94025, USA
[18] Centro de Investigaciones Energéticas, Medioambientales y Tecnológicas (CIEMAT), Madrid, Spain
[19] Cerro Tololo Inter-American Observatory, NSF's National Optical-Infrared Astronomy Research Laboratory, Casilla 603, La Serena, Chile
[20] Instituto de Física Teórica, Universidade Estadual Paulista, São Paulo, Brazil
[21] CNRS, UMR 7095, Institut d'Astrophysique de Paris, F-75014, Paris, France
[22] Sorbonne Universités, UPMC Univ Paris 06, UMR 7095, Institut d'Astrophysique de Paris, F-75014, Paris, France
[23] Department of Physics & Astronomy, University College London, Gower Street, London, WC1E 6BT, UK
[24] Institut de Física d'Altes Energies (IFAE), The Barcelona Institute of Science and Technology, Campus UAB, E-08193 Bellaterra (Barcelona), Spain
[25] Astronomy Unit, Department of Physics, University of Trieste, via Tiepolo 11, I-34131 Trieste, Italy
[26] INAF-Osservatorio Astronomico di Trieste, via G.B. Tiepolo 11, I-34143 Trieste, Italy
[27] Institute for Fundamental Physics of the Universe, Via Beirut 2, I-34014 Trieste, Italy
[28] Department of Physics, IIT Hyderabad, Kandi, Telangana 502285, India
[29] Faculty of Physics, Ludwig-Maximilians-Universität, Scheinerstr. 1, D-81679 Munich, Germany
[30] Department of Physics and Astronomy, University of Pennsylvania, Philadelphia, PA 19104, USA
[31] Santa Cruz Institute for Particle Physics, Santa Cruz, CA 95064, USA
[32] Institute of Theoretical Astrophysics, University of Oslo, P.O. Box 1029, Blindern, NO-0315 Oslo, Norway
[33] Institut d'Estudis Espacials de Catalunya (IEEC), E-08034 Barcelona, Spain
[34] Institute of Space Sciences (ICE, CSIC), Campus UAB, Carrer de Can Magrans, s/n, E-08193 Barcelona, Spain
[35] Kavli Institute for Cosmological Physics, University of Chicago, Chicago, IL 60637, USA
[36] Instituto de Fisica Teorica UAM/CSIC, Universidad Autonoma de Madrid, E-28049 Madrid, Spain
[37] Department of Astronomy, University of Michigan, Ann Arbor, MI 48109, USA
[38] Department of Physics, University of Michigan, Ann Arbor, MI 48109, USA
[39] School of Mathematics and Physics, University of Queensland, Brisbane, QLD 4072, Australia
[40] Center for Cosmology and Astro-Particle Physics, The Ohio State University, Columbus, OH 43210, USA
[41] Department of Physics, The Ohio State University, Columbus, OH 43210, USA
[42] Center for Astrophysics | Harvard & Smithsonian, 60 Garden Street, Cambridge, MA 02138, USA
[43] Australian Astronomical Optics, Macquarie University, North Ryde, NSW 2113, Australia
[44] Lowell Observatory, 1400 Mars Hill Road, Flagstaff, AZ 86001, USA
[45] Departamento de Física Matemática, Instituto de Física, Universidade de São Paulo, CP 66318, São Paulo, SP, 05314-970, Brazil
[46] George P. and Cynthia Woods Mitchell Institute for Fundamental Physics and Astronomy, and Department of Physics and Astronomy, Texas A&M University, College Station, TX 77843, USA
[47] Department of Astrophysical Sciences, Princeton University, Peyton Hall, Princeton, NJ 08544, USA
[48] Institució Catalana de Recerca i Estudis Avançats, E-08010 Barcelona, Spain
[49] Institute of Astronomy, University of Cambridge, Madingley Road, Cambridge, CB3 0HA, UK
[50] Hamburger Sternwarte, Universität Hamburg, Gojenbergsweg 112, D-21029 Hamburg, Germany

[51] School of Physics and Astronomy, University of Southampton, Southampton, SO17 1BJ, UK
[52] Computer Science and Mathematics Division, Oak Ridge National Laboratory, Oak Ridge, TN 37831, USA
[53] Institute of Cosmology and Gravitation, University of Portsmouth, Portsmouth, PO1 3FX, UK
[54] Max Planck Institute for Extraterrestrial Physics, Giessenbachstrasse, D-85748 Garching, Germany
[55] Universitäts-Sternwarte, Fakultät für Physik, Ludwig-Maximilians Universität München, Scheinerstr. 1, D-81679 München, Germany
Received 2021 October 5; revised 2021 December 17; accepted 2021 December 25; published 2022 March 9

Abstract

We report the combined results of eight searches for strong gravitational lens systems in the full 5000 square degrees of Dark Energy Survey (DES) observations. The observations accumulated by the end of the third observing season fully covered the DES footprint in five filters (*grizY*), with an *i*-band limiting magnitude (at 10σ) of 23.44. In four searches, a list of potential candidates was identified using a color and magnitude selection from the object catalogs created from the first three observing seasons. Three other searches were conducted at the locations of previously identified galaxy clusters. Cutout images of potential candidates were then visually scanned using an object viewer. An additional set of candidates came from a data-quality check of a subset of the color–coadd tiles created from the full DES six-season data set. A short list of the most promising strong-lens candidates was then numerically ranked according to whether or not we judged them to be bona fide strong gravitational lens systems. These searches discovered a diverse set of 247 strong-lens candidate systems, of which 81 are identified for the first time. We provide the coordinates, magnitudes, and photometric properties of the lens and source objects, and an estimate of the Einstein radius for 81 new systems and 166 previously reported systems. This catalog will be of use for selecting interesting systems for detailed follow up, studies of galaxy cluster and group mass profiles, as well as a training/validation set for automated strong-lens searches.

Unified Astronomy Thesaurus concepts: High-redshift galaxies (734); Strong gravitational lensing (1643)

Supporting material: machine-readable tables

1. Introduction

Gravitational lensing occurs when the gravitational field of a massive foreground object, the lens, deflects the light of a more distant object, the source. If the lens is massive enough, and the source, lens, and observer are sufficiently collinear and distant from one another, the observed image of the source object can be distorted into rings, arcs, or multiple images. This effect is known as strong gravitational lensing (SL), and has become a powerful and popular tool for studying a wide variety of extragalactic physics and cosmology.

Though SL of very distant objects by foreground galaxies was predicted (Zwicky 1937) four decades prior, the first discovery of a strongly lensed object was that of QSO 0957 +561 (Walsh et al. 1979), a double image of a single quasar at a redshift of $z = 1.4$. Not long after, it was realized that the long, narrow, and curved features bent around the centers of galaxy clusters were actually SL systems as well (Soucail et al. 1987; Grossman & Narayan 1989; Lynds & Petrosian 1989). In the subsequent 40-year interval, the count of candidate strongly lensed galaxies has expanded to more than 2000. At the same time, so has their scientific interest.

SL provides new opportunities to study astrophysics and the physics of dark matter. Because the surface brightness of a source galaxy is unchanged by lensing, magnification of the source provides amplification of the image flux. Colloquially named "Einstein's Telescopes" (Gates 2010), strong-lens systems enable studies of the details of distant galaxies that would otherwise be unresolved or too faint. For example, faint lensed sources with relatively large redshifts enable studies of the initial mass-to-light ratio, star formation, and metallicity in young galaxies (e.g., Bayliss et al. 2014; Leier et al. 2016). Studies of the lens systems, whether galaxies, galaxy groups, or galaxy clusters, provide information on their total mass and mass profiles, including baryon and dark matter (e.g., Koopmans et al. 2009; Wiesner et al. 2012; Newman et al. 2015; Treu & Ellis 2015), and explore the connection between these characteristics and the occurrence of strong lensing (Robertson et al. 2020; Fox et al. 2021; Sonnenfeld & Cautun 2021). Strong-lens systems are now being used to study galaxy and cluster substructures and to, in turn, constrain the interaction physics of dark matter (Meneghetti et al. 2020; Gilman et al. 2021).

SL enables studies of cosmology. Studies of the characteristics of ensembles of strong-lensing systems can be used to constrain Ω_M in wCDM and ΛCDM (Leaf & Melia 2018), albeit loosely, with samples of O(100) confirmed lensing systems. Studies of gravitationally lensed time-varying systems (Refsdal 1964; Blandford & Narayan 1992; Birrer et al. 2016; Oguri 2019), such as lensed quasars (Schechter et al. 1997; Suyu et al. 2013) or supernovae (Grillo et al. 2018), are used to constrain the expansion history between the source, lens, and observer.[56] Individual measurement of strongly lens quad quasars systems provide (Bonvin et al. 2017; Shajib et al. 2020) constraints on H_0 with about 4% precision, and combinations (Suyu et al. 2017; Wong et al. 2020) are now in mild tension, or not (Birrer et al. 2020), with early universe probes, depending (Birrer & Treu 2021) on assumptions of the lens' radial mass profiles. Lens systems with multiple sources at differing redshifts can provide (Link & Pierce 1998; Gavazzi et al. 2008; Collett et al. 2012) complementary information about the expansion history, independent of the Hubble constant. Constraints on Ω_M and the dark energy equation of state, w, are at about the 20% level from individual lensing

Original content from this work may be used under the terms of the Creative Commons Attribution 4.0 licence. Any further distribution of this work must maintain attribution to the author(s) and the title of the work, journal citation and DOI.

[56] Note that our SL searches could identify lensed quasars, but it is unlikely that we would have identified short duration transients, such as supernovae, in our wide-field images.

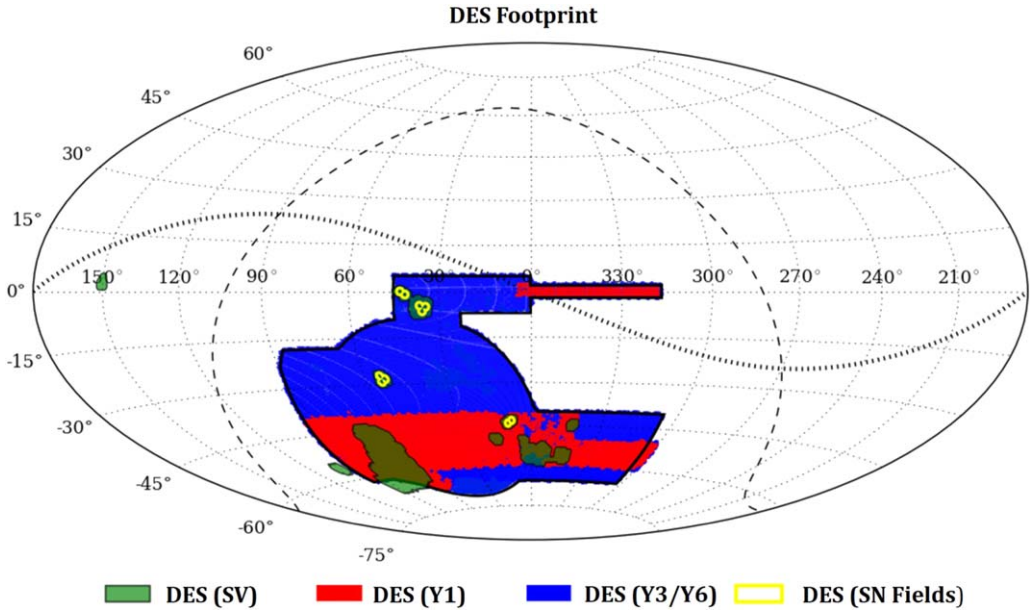

Figure 1. The footprint of the DES. This result is based on searches of the DES Y3/Y6 footprint, outlined in black. Note that the DES Y3 footprint included additional observations of the Y1 and SV fields, and the Y6 footprint included additional observations in all of those.

Table 1
Comparison between the Y1, Y3, and Y6 Catalogs

Parameter	Y1	Y3	Y6
Sky coverage, *grizY* intersection (deg^2)	1793	5186	4913
Objects (galaxies/stars)	137M total	310M/80M	543M/145M
i-band uniformity (typical number of exp.)	3 to 4	4 to 6	8 to 10
i-band single-epoch median point-spread function FWHM (″)	0.97	0.88	0.88
Coadd median astrometric relative precision (ang. dist., mas)	25	30	27
i-band coadd mag. Lim. (MAG_AUTO)	22.5	22.5	23.1
i-band coadd mag. Lim. (MAG_APER_4, 1.″95 diam.)	22.9	23.4	23.8

Note. Magnitude limits are given for detections with a signal-to-noise ratio (S/N) $\geqslant$ 10.

systems (Jullo et al. 2010; Collett & Auger 2014). In these systems it can be critical to accurately model massive lens substructures to obtain unbiased cosmological constraints (D'Aloisio & Natarajan 2011).

The count of candidate SL systems has increased rapidly with the advent of deep wide-field surveys with dedicated SL searches. In the Canada–France–Hawaii Telescope Legacy Survey (CFHTLS) Strong Lensing Legacy Survey (Cabanac et al. 2007), 54 systems with promising lenses were identified by the ARCFINDER algorithm (More et al. 2012) in 150 square degrees, 49 confirmed strong-lens systems identified with RINGFINDER (Gavazzi et al. 2014), and 29 promising and 59 total (More et al. 2016) from a crowdsourcing (Marshall et al. 2016) effort. CFHTLS imaging yielded 16 more probable to definite SL systems using neural-network-based searches (Jacobs et al. 2017). The Survey of Gravitationally lensed Objects in Hyper Suprime Cam (HSC) Imaging (SuGoH; Sonnenfeld et al. 2018) used three different methods, including YATTA LENS, to search the Hyper Suprime Cam Subaru Strategic Program (HSC SSP) images. The program yielded 333 galaxy–galaxy SL candidates from an area of 442 deg^2. The Kilo Degree Survey images were searched using machine-learning (ML) classifiers that discovered 227 high-grade SL candidates, plus an additional 200 candidates discovered serendipitously (Petrillo et al. 2017, 2019; Li et al. 2020). Cañameras et al. (2020) discovered 330 new SL systems in the 30,000 square degree Panoramic Survey Telescope and Rapid Response System (Pan-STARRS) 3π Survey (Chambers et al. 2016). The 1.64 deg^2 Hubble Space Telescope (HST) Cosmic Evolution Survey (COSMOS) field yielded 67 galaxy–galaxy lens candidates (Faure et al. 2008). HST was also used to confirm a total of 110 SL systems identified (Bolton et al. 2008; Shu et al. 2017) in the Sloan Digital Sky Survey (SDSS) spectroscopic data. SDSS also yielded 19 confirmed systems to the Sloan Bright Arcs Survey (Allam et al. 2007; Diehl et al. 2009; Kubo et al. 2009, 2010; Lin et al. 2009), and more than 30 confirmed and 50 additional candidate lenses to the Cambridge And Sloan Survey of Wide Arcs in the Sky (CASSOWARY) survey (Belokurov et al. 2009; Pettini et al. 2010; Stark et al. 2013). Searches of galaxy clusters identified in SDSS yielded 16 strong-lens systems with >10″ radius and 21 additional SL candidates (Hennawi et al. 2008), 68 giant arcs in Wen et al. (2011), 10 SL systems in Furlanetto et al. (2013b), and 37 more in Sharon et al. (2020). More recently, a search of galaxy clusters in HSC imaging (Jaelani et al. 2020) revealed more than 600 candidate strong-lens systems, of

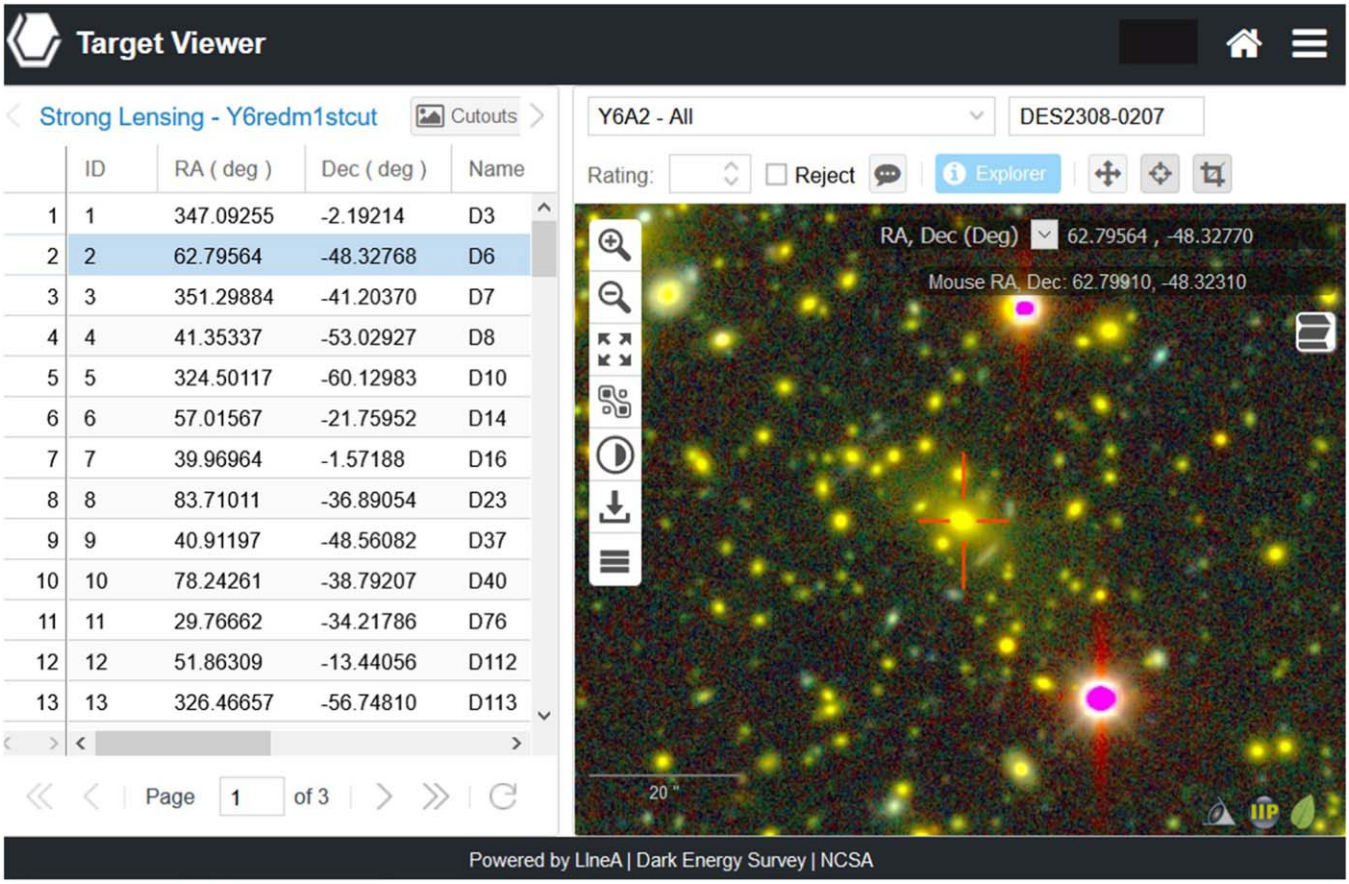

Figure 2. An example of an SL candidate shown in the Target Viewer. The left panel is a list of cutouts and characteristics, such as the R.A. and decl. On the right side of the viewer is the optical image as well as some of the controls for manipulating the viewer. One cutout is displayed at a time, with an adjustable size of about 2′ on a side. In addition, the Target Viewer can access DES object catalogs and encircle the identified objects (not shown). Each circle can display useful information about the object, including the OBJECTID, which provides reference to the object in the respective data release.

which 8 are confirmed spectroscopically. The Extended Baryon Oscillation Spectroscopic Survey (eBOSS) spectroscopic data produced (Talbot et al. 2021) 838 likely galaxy–galaxy SL systems with an Einstein radius $\lesssim 1''$. The Dark Energy Spectroscopic Instrument (DESI) Legacy Imaging Surveys team used 14,000 square degrees of images from several instruments, including the Dark Energy Camera (Flaugher et al. 2015), in combination with a neural network trained on real SL systems, to identify 1545 candidate systems (Huang et al. 2020, 2021).

Galaxy clusters, among the most massive objects in the universe, are ideal candidates for strong lenses, and optical observations of galaxy cluster catalogs have yielded many SL systems. Galaxy cluster catalogs selected via optical observations, the Sunyaev–Zel'dovich effect (Sunyaev & Zeldovich 1972), or as extended high-flux X-ray sources have been used. Follow-up of South Pole Telescope (SPT; Reichardt et al. 2013) detections yielded 34 new and 10 previously known SL systems in Bleem et al. (2015), and 44 new SL systems in Bleem et al. (2020). Follow up of Atacama Cosmology Telescope (ACT) galaxy cluster identifications (Hilton et al. 2021) yielded 67 new candidates including many in the Dark Energy Survey (DES) footprint that are characterized here for the first time.

The DES data have proven to be a productive source of SL candidate systems. Searches for lensed quasars have yielded four spectroscopically confirmed systems (Agnello et al. 2015; Lin et al. 2017; Ostrovski et al. 2017), two new quad SL systems, and 96 more quasar lens candidates ripe for spectroscopic follow up (Agnello & Spiniello 2019). Spectroscopic observations by the Strong-lensing Insights into Dark Energy Survey (STRIDES) collaboration confirmed 10 new lensed quasars and 10 quasar pairs (Lemon et al. 2020). Visual scanning of 400,000 color cutout images at coordinates selected, using techniques similar to those of this paper, from the ∼250 square degree science verification (SV) and ∼1800 square degree Y1 catalogs yielded 348 new SL candidates in Diehl et al. (2017), as well as one serendipitous SL discovery (Bettinelli et al. 2016). The convolutional neural-network-based search technique described in Jacobs et al. (2017) contributed (Jacobs et al. 2019a, 2019b) 485 ranked candidates in the full ∼5000 square degree DES footprint, principally of the galaxy–galaxy lens configuration. The latter paper also included 26 additional SL candidates identified by visual scanning of ∼54,000 potential lensing targets identified using procedures similar to those of Diehl et al. (2017). Spectroscopic confirmation of 17 DES systems is described in Nord et al. (2016, 2020), Lin et al. (2017), and Collett et al. (2017).

The recent competitive success of automated and machine-learning methods for identifying strong-lens candidates is evident from a simple comparison of the numbers of candidates in these references. Neural network and machine-learning algorithm searches for SL systems have advanced because of increased attention to the techniques power and capabilities.

Advances in computer vision have given rise to automated searches for strong-lens candidates, and for classification, deblending, and modeling of strong-lens candidates (Alard 2006; Seidel & Bartelmann 2007; Kubo & Dell'Antonio 2008; Furlanetto et al. 2013a; Joseph et al. 2014; Li et al. 2016; Paraficz et al. 2016; Xu et al. 2016; de Bom et al. 2017; Lanusse et al. 2018; Metcalf et al. 2019; Plazas 2020). Nonetheless, these machine-learning searches continue to benefit from visual scanning and the ranking of candidate systems. Furthermore, continued efforts to attain large samples of real lenses with a variety of morphologies is important for training and validation of new automated lens-finding algorithms, particularly for the identification of group- and cluster-scale SL systems, where machine learning has been less successful.

In this paper we report 247 strong gravitational lens candidates from searches of the full 5000 square degree DES footprint, including 81 previously unreported candidates. These lenses constitute a diverse set of primarily galaxy group- and cluster-scale systems, with both red and blue sources. We provide details of the locations (R.A. and decl.), and the g, r, i, z, and Y band magnitudes of source and lens objects, as well as Einstein radii and a rank, quantifying the confidence level of the selection, for each SL candidate system. This paper is organized as follows. In Section 2 we describe the DES observations and catalogs. In Section 3 we describe our strong gravitational lens search procedures. In Section 4 we describe the results from the searches and provide the properties of the candidate lens systems. We highlight some of the systems that have notable properties. Finally, in Section 5 we summarize and discuss our results.

2. Dark Energy Survey Imaging Data

The DES has completed a six-season program that imaged 5100 square degrees of the southern galactic cap using the Dark Energy Camera (DECam; Flaugher et al. 2015), which is operated on the 4 m Victor M. Blanco Telescope at Cerro Tololo Inter-American Observatory (CTIO) near La Serena, Chile. Following an SV period (Dark Energy Survey Collaboration et al. 2016), DES data collection typically occurred from mid-to-late August to mid-February, starting on 2013 August 31 and ending on 2019 January 9. Over the 6-year survey, we accumulated 10 high-quality, 90 s duration observations of the full survey field in each of the four filter g, r, i, and z bands, and 6 to 10 high-quality observations of 45 or 90 s length for the Y band (totaling 450 s). In addition to the wide-field survey, DES performed a time-domain supernova survey during the same time period, visiting 10 fields in the g, r, i, and z-band filters with an approximately weekly cadence and at much greater depth (Kessler et al. 2015) than the wide-field survey. Details of the observation strategy, survey operations, and the survey progress for each of the seasons are available (Diehl et al. 2016, 2018, 2019; Neilsen et al. 2019). Most of the searches described in this paper used the object catalogs and images from the first three seasons of observations as starting points. Much of the information that we provide about the candidate strong-lens systems comes from the full six-season data set. When we refer to Y1 (Drlica-Wagner et al. 2018), Y3 (Abbott et al. 2018), and Y6 (Dark Energy Survey Collaboration et al. 2021) data sets, we mean to include all the preceding seasons of observations. For instance, Y3 refers to the data from the first three seasons.

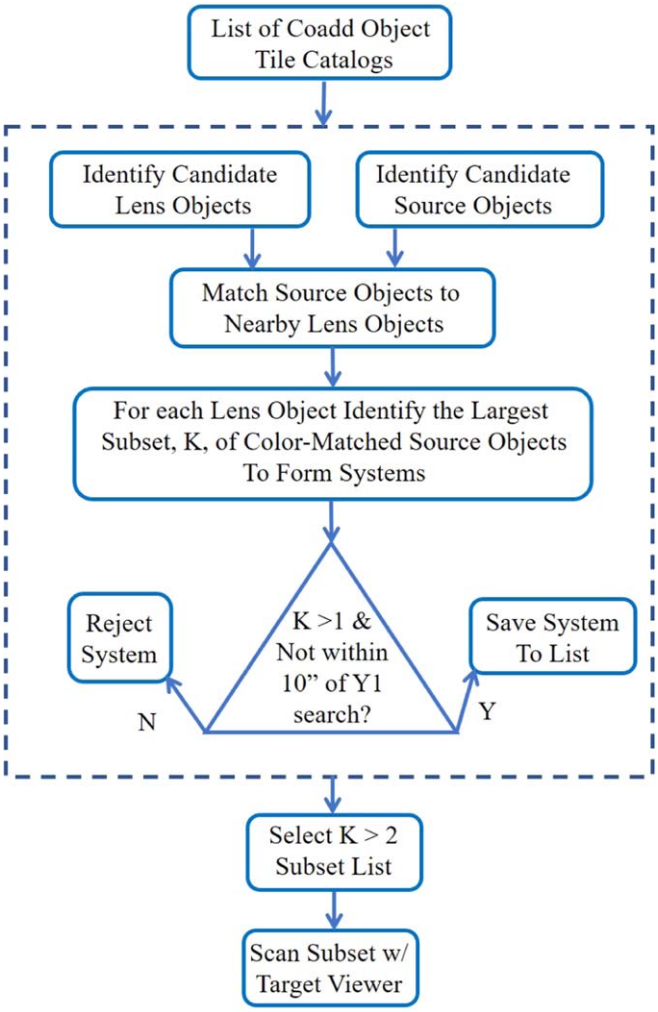

Figure 3. Typical flowchart for the BNA and RNA search algorithms. The box with the dotted outline is a single computer program. At the last step within the program, "Y" and "N" stand for "yes" and "no." The K > 2 subset selection was done on three of four of these searches.

The observations were processed by the Dark Energy Survey Data Management (DESDM) system (Mohr et al. 2012; Morganson et al. 2018) in three pipelined stages: single-epoch detrending, photometric calibration, and coaddition. The detrending operation removes the instrumental signature, subtracts the sky background, and removes artifacts such as cosmic rays from the individual exposures. The resulting images are in FITS-formatted files with an inverse-variance weight (WGT), and a mask of bad pixels (MSK). Single-epoch catalogs were produced using PSFEx (Bertin 2013) and Source-Extractor (SExtractor; Bertin & Arnouts 1996). Astrometric calibration is performed by matching bright stars on each exposure to reference stellar catalogs (Two Micron All Sky Survey (2MASS; Skrutskie et al. 2006) for Y3, and the Gaia Data Release 2 (DR2; Gaia Collaboration et al. 2018) for Y6) using SCAMP (Bertin 2006). Magnitude zero-points for each CCD on each exposure are determined using the Forward Global Calibration Method (Burke et al. 2018). Finally, exposures in each filter were coadded using SWarp (Bertin 2010) in 10,000 by 10,000 pixel tiles 0°.72 on a side. SExtractor was then run on a weighted combination of coadded $r+i+z$ detection tiles to form catalogs of objects, and then rerun on the individual filter bands at the location of the detected objects.

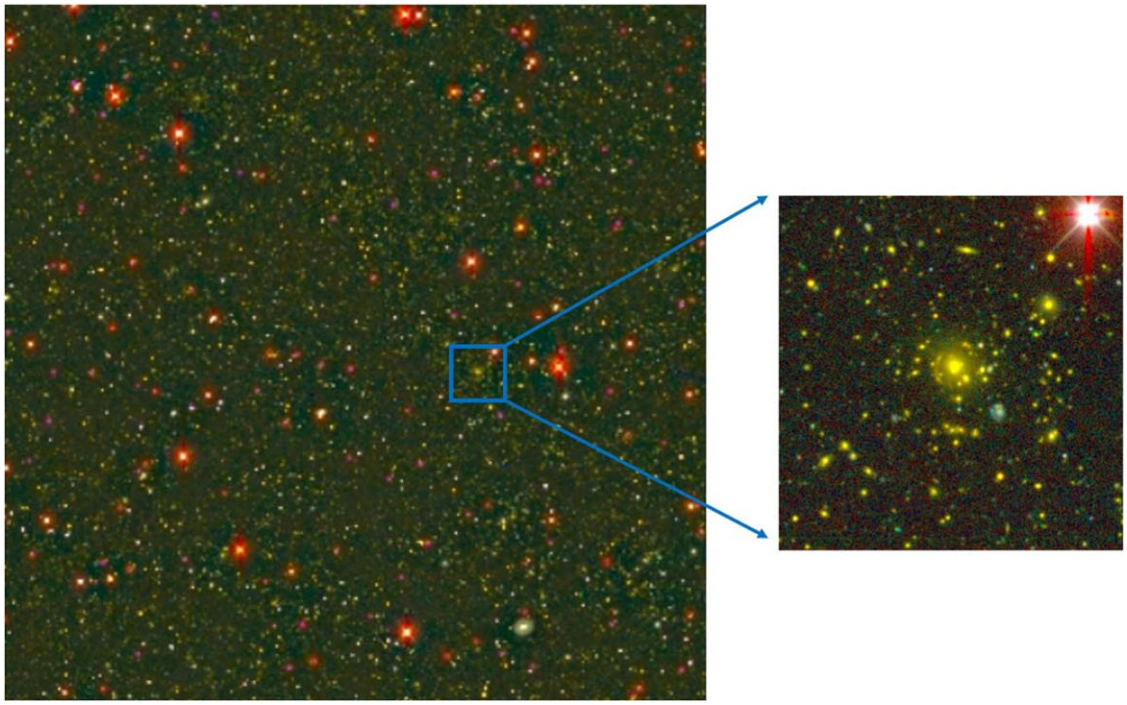

Figure 4. In the visual data-quality test, we first displayed the full tile of DES data, 0.72 deg on each side (left). Then we zoomed-in a factor of 50–100 (in area) at roughly a dozen places on each tile, looking for problems noticeable in a cutout roughly 5′ on a side. If we noticed a potential SL candidate we recorded its position. The right side is about one-fourth of our typical zoomed-in area, but at the scale that we viewed it.

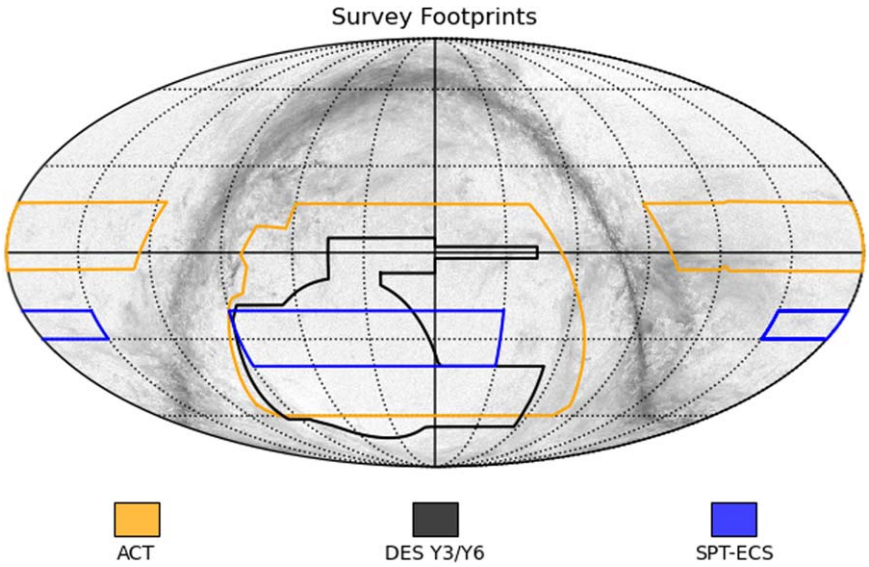

Figure 5. The footprints of the DES and other cluster catalogs referenced in this work. The DES redMaPPer catalogs span the DES footprint, outlined in black in the center. Searches were also conducted based on galaxy cluster catalogs from the SPTPol-ECS and ACT, whose footprints are shown in blue and orange, respectively. The background dust map was obtained from Planck Data Release 2. The overlap between the DES and ACT cluster footprints is approximately 4770 square degrees, and the overlap between the SPT and DES footprints is approximately 1510 square degrees. The intersection of all three footprints is approximately 1470 square degrees.

The separation or deblending of closely positioned (or even overlapping) objects is a challenge where the goal is to balance completeness against the spurious separation of features within a single galaxy. The deblending was performed using the detection images. For Y6, the SExtractor source detection threshold was lowered from 10σ (in Y3) to 5σ to detect fainter sources; this was accompanied by a reoptimization of the deblending parameters. As a result, objects are sometimes detected and/or deblended better in one data release than they are in the other. The absolute photometric calibration for both Y3 and Y6 is tied to the spectrophotometric Hubble CALSPEC standard star C26202 (Bohlin et al. 2014). Other differences between the Y3 and Y6 processing are described in Dark Energy Survey Collaboration et al. (2021). All of the previous seasons' observations were reprocessed to produce the new data sets. Each time, the object catalogs containing the list of objects, their shapes, and their astrometric and photometric properties were calculated for each coadd tile. Unless noted

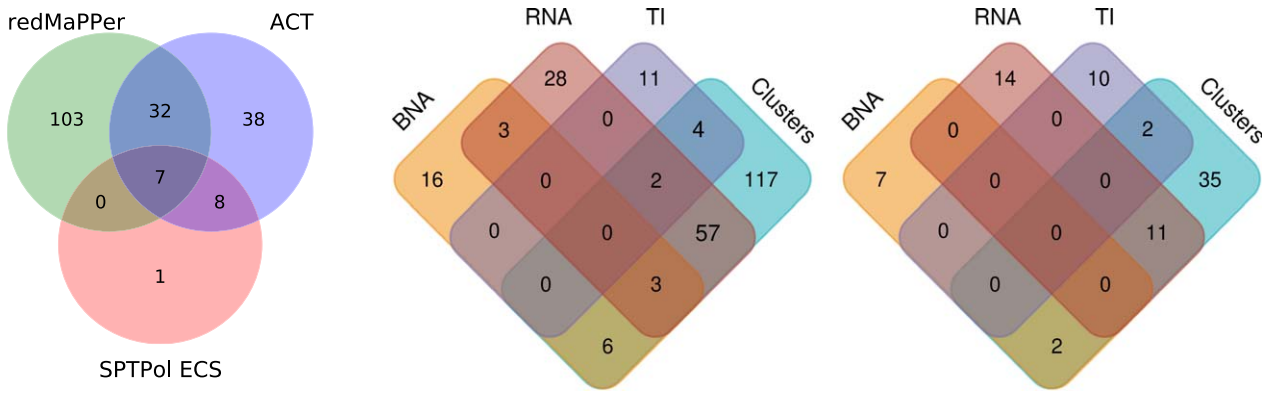

Figure 6. The systems presented in this work, sorted by the algorithms that identified them. Left: a breakdown of the galaxy cluster subset, showing how many systems were identified in redMaPPer, ACT, and SPTPol ECS searches. Center: all 247 systems presented in this work. RNA and BNA include both the RNA and BNA searches, TI are systems found serendipitously in tile inspections, and Clusters includes redMaPPer, ACT, and SPTPol ECS catalogs. Right: all 81 newly identified systems presented in this work.

Table 2
Summary of the Number of Objects Visually Scanned, the Number Ranked, and the Count of Those with a Rank ⩾3 for the Various Searches

Search	# Scanned	# Ranked	# Rank ⩾ 3	# New
BNA 3+	30319	95	21	6
BBNA 2+	18985	8	7	3
BNA combined		103	28	9
RNA 3+ No. 1	30994	110	91	25
RNA 3+ No. 2	5100	4	3	1
RNA combined		114	93	25
Tile inspection	4085	44	17	12
RedMapper	21092	152	142	35
ACT	1857	93	85	21
SPTPOL	325	17	16	2
Clusters combined		202	189	50
Totals			247	81

Note. We kept track of overlaps between searches for the columns "# Rank ⩾3" and "# New," but not for the columns "# Scanned" and "# Ranked." Where there are empty fields, we have not kept track of the distinct counts. Note that a single "New" system can be discovered by multiple searches. Therefore the subtotals and "Totals" can be less then the sums of the respective columns.

otherwise, the SExtractor MAG_AUTO magnitudes are the primary measures of the coadd flux used in further analysis.

Photometric redshifts (photo-z's) are derived by the Directional Neighbourhood Fitting (DNF) algorithm (De Vicente et al. 2016). The lens photo-z's are reasonably well estimated, given that our lens samples consist predominantly of red galaxies, which have strong 4000 Å break features that yield better photo-z measurements. However, we caution that our sources, which are typically fainter blue objects, will have photo-z's that are subject to larger uncertainties and systematic errors.

The DES Y1 and Y3/Y6 observing footprints are described in Dark Energy Survey Collaboration et al. (2016) and are shown in Figure 1. Table 1 characterizes these data sets for comparative purposes. Additional information about the SV (SVA1) data can be found in Diehl et al. (2017).

3. Gravitational Lens Candidate Search Procedures

We completed eight different searches, described below, to identify candidate strong-lens systems using the Y3 and Y6 data. One of the searches was a by-product of the Y6 data-quality effort. The seven other searches involved identifying and visually scanning a list of potential SL systems. While the origin of the lists was different for each search (those details are described below), the rest of the procedure is in common. The lists were loaded into the DES Science Portal (Dark Energy Survey Collaboration et al. 2021), which includes the Target Viewer, a tool for visualizing the DES fields that can also provide catalog information about the objects. The Target Viewer produced five-color (g-, r-, i-, z-, and Y-band) cutout images, roughly 2′ across, with one system centered on each page. Cutouts were scanned by either scientists with experience identifying strong-lens systems or students trained to do so. Each page required only a few seconds to scan. Figure 2 shows a sample page as seen on the Target Viewer. Potential SL candidates were identified by the occurrence of an apparent arc, or a pattern of arc-like knots or objects suggestive of an instance of strong lensing. It was not required that the potential sources or lenses that we identified were part of the selection that caused the cutout to be made in the first place. Interesting candidates were flagged for further evaluation. Some bright or particularly interesting candidates were immediately designated for further study.

Each search discovered new SL candidate systems. Some new systems were found by more than one of our searches, as well as some that had previously been discovered. After each search was completed, a short list of systems identified as candidates was compiled and all re-ranked by a team of five scientists. Each person assigned a score of 0–2 to each system—0 points if the system was thought to not be a SL candidate, 1 point if it might be, and 2 points if the system was expected to be an instance of strong lensing. Scores from all judges were summed to produce a rank between 0 and 10. Systems with a rank of at least 3 were taken as the final list for this paper. The candidate rankings of 3–10 span the range from possible to probable to definite strong-lens systems with rankings consistent with those used in the Master Lens Database (Moustakas et al. 2012) and other graded samples of strong-lens candidates.

3.1. "Blue Near Anything" Knot Searches

We searched the DES Y3 catalogs for SL candidates using a "Blue Near Anything" (BNA) algorithm, originally motivated by Kubik (2007) and used extensively by Diehl et al. (2017). This algorithm is aimed at identifying star-forming Lyman

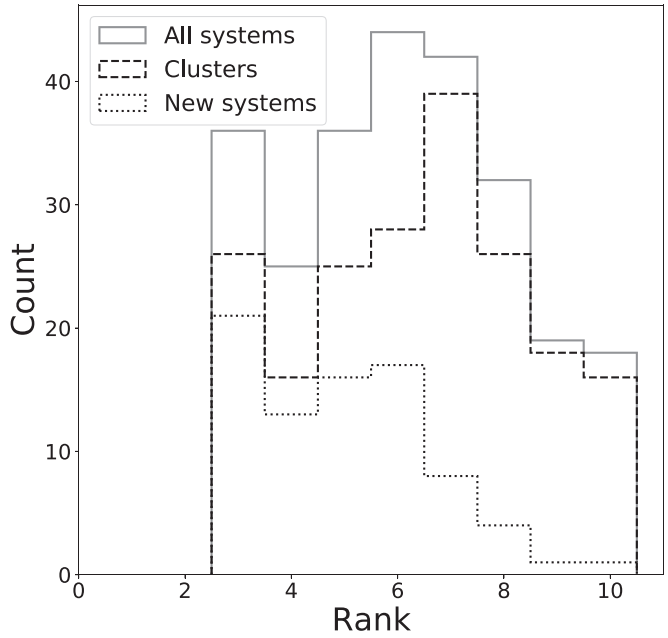

Figure 7. The rank of all systems presented in this work. The solid black line shows all systems, the dashed line shows the galaxy cluster's subset, and the dotted line shows newly discovered systems. The mean (median) rank of all systems presented is 6.12 (6).

break galaxies and Lyα emitting galaxies strongly lensed by massive luminous red galaxies. There were two such searches.

The first was performed on the single coadd tile object catalogs and is illustrated in Figure 3. First, a list of candidate lens galaxies was created. The criteria for a galaxy to be in the list of possible lenses are that at least one of the *r*-band, *i*-band, or *z*-band magnitudes is less than 21.5. Selection criteria on SExtractor outputs removed galaxies that were faint, objects that were not well deblended, objects that are likely to be stars, and artifacts left over from objects with saturated pixels. In each square degree tile, this search typically identified 5000–7000 candidate lens galaxies. Next, we formed a list of source candidates. The criteria for an object to be in the list of possible sources are that at least one of the magnitudes for the *g*-band, *r*-band, or *i*-band must also be less than 21.5 and that the object was not poorly deblended or contained saturated pixels. We did not apply star–galaxy separation in order to preserve strongly lensed quasars that appear star-like (Reed et al. 2015). Blue-colored source candidates were selected by requiring that $g-r<1.0$ and $r-i<1.0$. There were typically 2000–3000 candidate source objects per tile. Next, for each object in the lens list we identified the objects in the source list that were within 8″ of the lens. Then, we identified the largest set of those sources, associated with a given lens candidate object, that each had a similar color, where the similar requirement was that $|\Delta(g-r)|$ and $|\Delta(r-i)|$ both be less than 0.25 mag. This algorithm predominantly finds blue-colored source galaxies lensed by red galaxies or galaxy clusters, and we refer to it as the BNA 2+ selection. After we identified the list of candidates on each tile, we removed those candidates that were within 10″ of a position that we had previously scanned in the Y1 BNA search (Diehl et al. 2017). There were 247,076 systems that had 2 or more matched source objects in the 10,345 tile catalogs. We performed a visual scan of the 30,319 systems that had 3 or more matched source objects. This yielded a short list of 95 SL candidates.

The second BNA search was similar, but it was aimed at identifying those bright SL candidates that we might have missed by scanning only those systems with three or more blue knots. For this bright BNA (BBNA) selection, we raised the lens galaxy magnitude threshold to 20.5 and the source galaxy threshold to 20.0 and reran the algorithm. We performed a visual scan of the 18,985 resulting systems with two or more matched source objects. This yielded a short list of eight additional BBNA SL candidates, all of which received a rank of 3 or more.

3.2. "Red Near Anything" 3+ Knot Search

The motivation for this search, refereed to as "Red Near Anything" (RNA), was to discover SL systems with red-colored sources. It was similar to the RNA search used extensively for Y1 in Diehl et al. (2017), and similar to the BNA search described above except as noted. The lens candidate selection criteria required that any of *r*, *i*, $z<22.0$. In both iterations, there were two selection criteria for the source lists. The first was that any of *r*, *i*, $z<22.0$, that $g>23$, and that $g-r>0$ and $r-i>0$. The second was that any of *r*, *i*, $z<22.0$, that $g>23$ and $r>23$, and that $r-i>0$ and $i-z>0$. Again, a list of source candidates was matched against a list of lens candidates with an 8″ maximum radius. Next, for each system we found the largest set of matching sources for which $|\Delta(g-r)|<0.25$ and $|\Delta(r-i)|<0.25$. After eliminating candidates within 10″ of a location scanned in Diehl et al. (2017), there were 439,077 candidates. We visually scanned 30,994 targets with 3 or more source knots, short-listing 110 for further study.

We carried out the second iteration of this campaign on the Y3 data after we realized that the color-matching selection criterion $|\Delta(g-r)|<0.25$ would eliminate source objects that were *g*- and *r*-band dropouts. We reran the algorithm, this time requiring that $|\Delta(r-i)|<0.25$ and $|\Delta(i-z)|<0.25$. A total of 501,184 candidate systems remained after removing the locations we had checked in Diehl et al. (2017). There were 20,203 targets with 3 or more source knots. We visually scanned 5100 of them, finding four systems for the short list. Due to its low productivity, this search (RNA2) was abandoned before we scanned all the targets. All four of these had a grade of 3 or more.

3.3. An Undirected Search of DES Y6 Tiles

As part of the Y6A1 DES data release, we performed a data-quality check comprising a visual scan of a subset of the 10,167 1/2 square degree coadd tiles. The scanning took place in two stages. Initially 2377 tiles were scanned in R.A. order starting with R.A.s close to 0 hr. Later, we repeated the process on the 1708 tiles that did not had any targets in the BNA or RNA SL searches. We were looking for obvious quality defects such as the inclusion of problematic single exposures into the coadds. We identified coadds that included exposures that had been taken during an earthquake, some that had a trail from the reflections off the International Space Station, and others that had a subtle astrometric failures that resulted in a doubling up of the objects in one filter band. All of these bad exposures were removed from the data set, and coadds were remade without them. This visual scan procedure was as follows. First, we displayed the full coadd tile at a scale that permitted us to notice macroscopic problems, but not with a resolution to

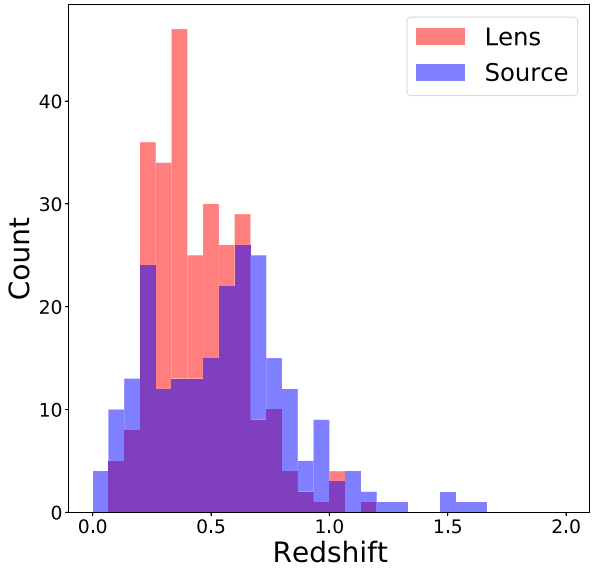

Figure 8. DESDM-calculated photometric redshifts for the sources and lenses. As explained in Section 2, the redshifts of the sources are subject to larger uncertainties and systematic errors.

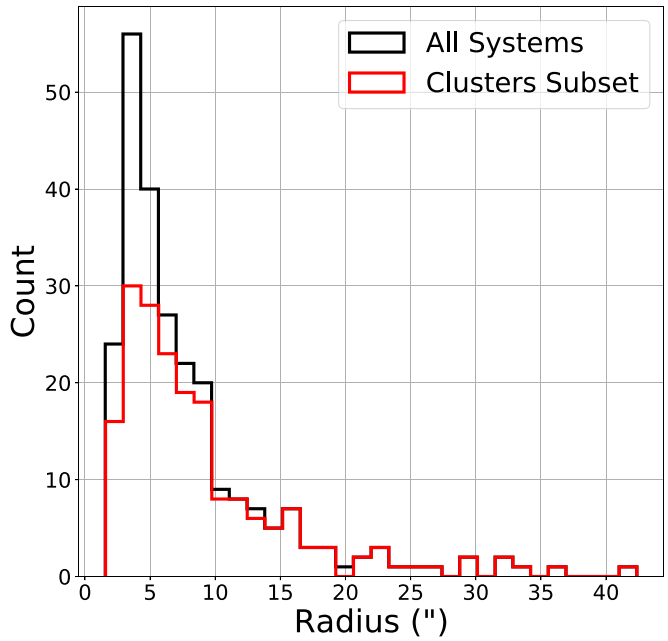

Figure 9. The binned distribution of Einstein radius estimates for the lens candidates. The cluster's subset, as defined in Figure 6, is shown separately, and accounts for nearly all systems with an Einstein radius above 10″.

notice SL systems. Then we zoomed in at a dozen or more different places on the coadd tile, looking for problems that could only be seen with finer resolution. See Figure 4. In this process we viewed only a fraction of the area of the tile, perhaps one-tenth, with sufficient resolution to spot a candidate SL system. We recorded 44 candidates for the short list. Seventeen of these were graded as rank 3 or more.

3.4. Scans of Galaxy Cluster Catalogs

Galaxy clusters are among the most massive structures in the universe, and form high-magnification regions where SL systems are likely to appear. We searched for SL systems in three catalogs of galaxy clusters: the optically selected DES Y3 redMaPPer catalog, and two cluster catalogs selected via the Sunyaev–Zel'dovich effect (Sunyaev & Zeldovich 1972): the ACT cluster catalog (Hilton et al. 2021) and the SPTPol Extended Cluster Survey catalog (Bleem et al. 2020). The overlap of all cluster catalog footprints is shown in Figure 5.[57] A Venn diagram of the how many SL systems were discovered in each cluster catalog can be found in Figure 6. Each catalog and their resulting SL systems are described in this section.

The red-sequence Matched-filter Probabilistic Percolation cluster finder algorithm (redMaPPer; Rykoff et al. 2014; McClintock et al. 2019; The Dark Energy Survey Collaboration et al. 2020) identifies galaxy clusters as overdensities of red-sequence galaxies in a catalog. The algorithm counts the excess number of red-sequence galaxies of similar colors that are brighter than a specified luminosity threshold within a circle with a of radius $R_\lambda = 1.0\ h^{-1}$ Mpc $(\lambda/100)^{0.2}$, where λ, the richness, is the number of galaxies in the cluster (Rozo et al. 2009). The galaxy cluster catalog used in this work was obtained from redMaPPer version 6.4.22+2 on DES Y3A2 Gold data (Sevilla-Noarbe et al. 2021). It is a volume-limited catalog with redshifts of the clusters ranging from $0.04 < z < 0.95$ and richness $\lambda > 5$. We visually scanned the 21,092 cluster sample with $\lambda > 20$ in this search. Though we have previously reported searches of the locations of $\lambda \geqslant 20$ redMaPPer clusters in the DES SV and Y1A1 fields (Nord et al. 2016; Diehl et al. 2017), respectively, we did not exclude those positions from this search. Of the 152 systems shortlisted for final grading, 143 were ranked $\geqslant$3.

The ACT cluster catalog identified more than 4000 galaxy clusters using the Sunyaev–Zel'dovich effect (Hilton et al. 2021). The full ACT data set (Naess et al. 2020) comprises 18,000 square degrees and overlaps the DES Y3 footprint almost completely. We visually scanned the 1857 ACT galaxy clusters within the DES footprint, identifying 93 for further evaluation and final grading. Of these, 77 were ranked $\geqslant$3. Some of these were already identified in Hilton et al. (2021).

The SPTPol Extended Cluster Survey (SPTPol-ECS; Bleem et al. 2020) identified 266 galaxy clusters with a detection significance $\chi > 5$, and 204 with $4 < \chi < 5$. The full DES footprint partially covered that of SPTPol-ECS. From the 470 total SPTPol-ECS galaxy cluster candidates, we scanned 325 locations in the DES Y6 data. Of these, 17 SL candidate systems were identified for final grading, and all 17 were ranked $\geqslant$3.

4. Search Results

The ranked lists from all searches were combined, yielding 247 SL systems with a rank of 3 or greater. Of these systems, 81 are presented for the first time. Figure 6 shows Venn diagrams illustrating the overlap between each search algorithm or catalog, for all 247 SL candidates and separately for the newly discovered systems. Table 2 shows the number of candidates searched and systems found for each subsearch. Figure 7 shows the distribution of the system ranks. Figures 8 and 9 show the lens and source photometric redshifts, and Einstein radii for the 247 SL systems. For strong lensing to occur, the source must be strictly more distant than the lens, yet in Figure 8 it is clear that some sources have a lower measured

[57] The dust map was obtained from Planck at http://irsa.ipac.caltech.edu/data/Planck/release_2/all-sky-maps/maps/component-maps/foregrounds/COM_CompMap_DustPol-commander_1024_R2.00.fits.

Table 3
Properties of All Candidate Lensing Systems, Ordered by Increasing R.A.

System Name	Rank	Algorithm	θ_E ($''$)	References
DESJ0002-3332	4	BNA	5.69 ± 0.83	…
DESJ0006-4208	10	ACT	7.70 ± 0.81	(B)
DESJ0007-4434	5	RedM	3.43 ± 0.43	(B), (D)
DESJ0011-4614	7	ACT, RedM	6.53 ± 2.35	(B), (D)
DESJ0014-0057	5	ACT, BNA, RedM missed	12.84 ± 1.31	SOGRAS J0014-0057 (h), (w)
DESJ0021-5028	3	RNA, RedM missed	3.87 ± 0.47	(B)
DESJ0025-3139	5	RedM	2.98 ± 0.40	(D)
DESJ0025-4946	6	RNA2	3.21 ± 0.41	DES J002510-494626 (A)
DESJ0026-4825	7	ACT, RedM	10.89 ± 0.26	…
DESJ0030-4507	7	RedM	9.71 ± 1.01	…
DESJ0031-4403	6	RNA	3.56 ± 0.44	DES J003104-440300 (A), (B)
DESJ0031-3717	5	RNA	4.53 ± 1.85	…
DESJ0032+0100	6	RNA, ACT, RedM	6.72 ± 0.51	HSCJ003217+010037 (w), (z)
DESJ0034+0225	10	RedM	13.22 ± 1.59	HSCJ003428+022522 (w), (z)
DESJ0035-2526	8	BNA	2.34 ± 0.35	(D)
DESJ0038-2155	3	BNA	5.64 ± 0.33	…
DESJ0040-4407	8	ACT, RedM missed	18.67 ± 1.89	(B)
DESJ0041-4155	7	BNA, ACT	7.23 ± 0.47	(B)
DESJ0042-6037	4	TI, RedM missed	9.19 ± 0.96	…
DESJ0043-6248	3	TI	3.22 ± 0.42	…
DESJ0043-2037A	9	TI, ACT, SPTPol	22.71 ± 4.16	SPT-CL J0043-2037 (m), (z)
DESJ0043-2037B	9	TI, ACT, SPTPol	16.69 ± 1.69	SPT-CL J0043-2037 (m), (z)
DESJ0043-3123	4	TI	3.85 ± 0.47	…
DESJ0043-3453	7	TI	3.90 ± 0.47	…
DESJ0044-0448	5	TI	2.86 ± 0.39	DESI-011.0219-04.8058 (v)
DESJ0044-0055	8	TI, RedM	7.63 ± 1.18	…
DESJ0045-0510	6	TI	3.58 ± 0.57	…
DESJ0045-2013	5	TI	2.09 ± 0.34	…
DESJ0045-0143	4	TI	1.56 ± 0.31	…
DESJ0045-5159	6	TI	3.43 ± 0.49	…
DESJ0046-0134	4	TI, RedM missed	7.40 ± 0.79	…
DESJ0047-5255	4	TI	4.26 ± 0.73	…
DESJ0047-3826	7	TI, ACT, RedM missed	7.88 ± 0.72	…
DESJ0048+0311	7	TI, RedM, RNA2	8.80 ± 0.72	RCSGA J004827+031114 (g), (D)
DESJ0057-4848	7	RNA, RedM	2.47 ± 0.36	(B)
DESJ0059-2800	4	RedM	7.28 ± 0.77	…
DESJ0100-3936	3	RedM	6.92 ± 1.07	…
DESJ0102-2911	8	RedM	4.89 ± 0.56	KiDS J010257.486-291121.76 (x), (z), (D)
DESJ0103-2234	3	RedM	9.17 ± 0.95	…
DESJ0103-1821	7	RedM	9.33 ± 0.97	DESI-015.8440-18.3629 (z)
DESJ0104-5341	7	RedM	2.53 ± 0.37	(B)
DESJ0105-3939	4	RedM	3.16 ± 0.41	(D)
DESJ0105-3520	3	RNA	2.24 ± 0.69	…
DESJ0106-3104	7	RedM	2.97 ± 0.40	KiDS J010606.232-310437.84 (x), (z)
DESJ0106-3700	3	ACT, RedM	5.92 ± 0.65	DESI-016.5369-37.0055 (z)
DESJ0106-5355	10	RNA, ACT, RedM	11.24 ± 2.08	(B)
DESJ0107-3128	10	BNA, RNA	5.04 ± 0.61	KiDS J010704.918-312841.03 (x), (z)
DESJ0109-3335	9	RedM	8.59 ± 0.90	(D)
DESJ0115-3520	3	RNA	4.99 ± 0.56	(D)
DESJ0120-5143	10	BNA	3.35 ± 0.49	DES J012042-514353 (A), (B), (D)
DESJ0128-2905	8	RedM	5.23 ± 0.58	LinKS 2323 (u)
DESJ0128-2957	5	RNA, RedM	3.67 ± 0.57	DESI-022.2123-29.9602 (z)
DESJ0129-1641	4	RNA, ACT	3.15 ± 0.41	…
DESJ0130-3744	7	BNA, RNA, RedM	5.33 ± 0.91	DES J013002-374457 (A), (D)
DESJ0131-1336	3	ACT, BBNA	22.78 ± 2.29	CLASH A209 (l)
DESJ0133-1650	3	BNA	5.70 ± 0.63	DESI-023.4239-16.8390 (z)
DESJ0133-6434	8	RNA, BBNA	4.44 ± 0.46	(D)
DESJ0134+0433	3	RedM	4.87 ± 0.55	DESI-023.6765+04.5639 (v)
DESJ0135-2328	4	ACT	6.39 ± 0.69	…
DESJ0135-2033	7	RedM	4.75 ± 0.60	DES J013542-203335 (A), (D)
DESJ0137-1034	4	BNA, RNA, ACT, RedM missed	13.95 ± 1.42	DESI-024.2940-10.5728 (z), (A)
DESJ0138-2155	10	ACT, SPTPol	18.18 ± 0.95	SPT-CL J0138-2155 (m)
DESJ0138-2844	8	RedM	3.54 ± 0.44	DESI-024.5974-28.7358 (z), (A), (D)
DESJ0142-5032	9	BNA, ACT	14.03 ± 0.64	(B)
DESJ0143-0850	6	RNA	2.47 ± 0.37	DES J014326-085021 (A), (C), (D)
DESJ0143-2617	4	RedM	5.80 ± 0.64	DESI-025.9390-26.2946 (z)
DESJ0144-2213	7	RNA, ACT, RedM, SPTPol	11.88 ± 1.22	SPT-CL J0144-2214 (m)
DESJ0145-0455	5	RNA	2.34 ± 0.35	CSWA 103 (i), (v), (y), (D)
DESJ0145+0137	3	RedM	10.13 ± 1.05	…
DESJ0145-3541	10	RedM	3.27 ± 0.42	DES J014546-354127 (A), (D)
DESJ0146-0929	10	ACT, RedM	12.05 ± 1.17	Hall's Arc (b), (i), (D)
DESJ0149-3825	6	ACT, SPTPol	9.42 ± 0.98	(D)

Table 3
(Continued)

System Name	Rank	Algorithm	θ_E ($''$)	References
DESJ0151-3544A	8	RNA, ACT, RedM, SPTPol	7.32 ± 0.78	SPT-CL J0151-3544 (m)
DESJ0151-3544B	8	RNA, ACT, RedM, SPTPol	29.34 ± 2.95	SPT-CL J0151-3544 (m)
DESJ0152-2853	3	ACT, SPTPol	16.42 ± 0.57	…
DESJ0154-2324	7	RedM	3.59 ± 0.30	DESI-028.6096-23.4067 (z)
DESJ0158-0040	6	RedM	3.52 ± 0.84	DESI-029.6032-00.6665 (v), (D)
DESJ0159-3413	10	ACT, RedM, SPTPol	10.39 ± 0.63	SPT-CL J0159-3413 (m), (D)
DESJ0200+0127	6	RNA, RedM missed	3.99 ± 0.48	…
DESJ0203-2338	7	BNA	3.86 ± 0.45	PS1J0203-2338 (y), (A), (C), (D)
DESJ0203-2017	7	RNA, ACT, RedM missed	5.95 ± 0.65	SPT-CL J0203-2017 (m)
DESJ0203-3104	6	RNA, RedM	2.37 ± 0.38	DESI-030.9153-31.0823 (z)
DESJ0205-3539	8	RedM	3.36 ± 0.43	(D)
DESJ0205-1935	6	RNA, ACT, RedM	4.30 ± 0.50	…
DESJ0206+0258	6	RNA, RedM	4.14 ± 0.49	…
DESJ0206-0114	5	RNA, ACT	2.22 ± 0.45	HSCJ020613-011417 (w), (D)
DESJ0207-2726	8	RedM	4.34 ± 0.69	DESI-031.7778-27.4457 (z), (D)
DESJ0209+0222	4	ACT, RedM	7.73 ± 0.82	HSCJ020937+022256 (w)
DESJ0209-3547	6	ACT, RedM	5.92 ± 0.65	DESI-032.4765-35.7990 (z)
DESJ0212-2842	3	RedM	6.47 ± 0.57	…
DESJ0214-0206	3	RNA	3.14 ± 0.43	HSCJ021408-020628 (w), (y), (D)
DESJ0214-0535	7	RedM	7.30 ± 0.82	SL2S J021408-053532 (a), (w)
DESJ0214-4207	4	RedM	2.45 ± 0.36	…
DESJ0218-3142	6	RNA, ACT, SPTPol, RedM missed	8.50 ± 0.89	…
DESJ0219-4427	6	RedM	3.87 ± 0.47	…
DESJ0219+0247	3	ACT, RedM missed	17.12 ± 1.73	HSCJ021953+024707 (w)
DESJ0220-3833	8	RedM	8.98 ± 2.14	DESI-035.2405-38.5511 (z), (D)
DESJ0225-4200	7	RNA	10.68 ± 1.10	…
DESJ0227-4516	7	RedM	3.99 ± 0.48	(B)
DESJ0229-3110	8	RedM	5.21 ± 0.58	KiDS J022956.259-311022.65 (x), (z), (A)
DESJ0230-2702	4	RNA, ACT, RedM missed	6.42 ± 0.69	…
DESJ0234-4529	3	BNA	3.64 ± 0.73	(B)
DESJ0237-3017	5	RNA, RedM	5.05 ± 0.57	DESI-039.3484-30.2921 (z)
DESJ0238-3334	5	BNA	3.73 ± 0.26	…
DESJ0239-0127	3	RedM	5.40 ± 0.92	DESI-039.9261-01.4632 (v), (w)
DESJ0239-0134	10	RNA, ACT, RedM	11.47 ± 1.12	A370 (t), (w), (D)
DESJ0242-2132	6	RNA	19.33 ± 0.47	…
DESJ0243-3843	7	RNA, ACT, RedM missed	15.20 ± 1.19	SPT-CL J0243-4833 (p)
DESJ0245-5301	6	ACT, RedM	6.21 ± 1.90	(D)
DESJ0248-0331	10	ACT	15.92 ± 0.46	CLASH A383 (l), (D)
DESJ0248-0216	10	ACT, RedM	14.21 ± 0.81	DESI-042.0371-02.2771 (z)
DESJ0248-3955	6	BNA	3.95 ± 0.40	(D)
DESJ0250-6308	8	RNA	4.19 ± 0.49	…
DESJ0251-5515	6	RedM	6.89 ± 0.74	(B)
DESJ0252-4732	7	RedM	2.94 ± 0.39	(B), (D)
DESJ0252-1459	6	RedM	3.44 ± 0.43	…
DESJ0253-2629	5	RedM	4.66 ± 0.54	…
DESJ0257-2209	5	RNA, ACT, SPTPol	1.83 ± 0.32	SPT-CL J0257-2209 (m), (z)
DESJ0304-4921	10	ACT, RedM	25.42 ± 0.95	(B), (D)
DESJ0307-5042	5	ACT, RedM missed	11.57 ± 1.00	(B), (D)
DESJ0309-3805	5	RedM	1.71 ± 0.31	DES J030920-380545 (A), (D)
DESJ0310-4647	8	RNA, ACT	9.49 ± 0.37	SPT-CL J0310-4647 (g), (B), (D)
DESJ0311-4232	6	RNA, RedM missed	5.13 ± 0.58	(D)
DESJ0315-5954	8	RedM	8.84 ± 0.92	…
DESJ0316-4816	4	BNA	3.01 ± 0.48	(B)
DESJ0317-4421	3	ACT	7.81 ± 0.82	…
DESJ0327-1326	10	RNA, ACT, RedM	16.01 ± 2.69	RCSGA 032727-132609 (d), (D)
DESJ0328-2140	6	RNA, ACT, RedM, SPTPol	21.14 ± 3.23	(D)
DESJ0330-5228	9	TI, ACT, RedM	6.21 ± 0.27	DES J0330-5228 (o), (B), (D)
DESJ0334-1311	6	RedM	6.84 ± 1.16	DESI-053.6254-13.1866 (z)
DESJ0336-3812	3	RedM	1.58 ± 0.31	(D)
DESJ0339-4849	5	ACT, RedM	12.65 ± 1.10	(B)
DESJ0339-3856	5	RNA, RedM	1.85 ± 0.32	DESI-054.8226-38.9498 (z)
DESJ0339-3313	5	RedM	11.85 ± 1.21	…
DESJ0341-5130	8	RedM	2.58 ± 0.37	(B), (D)
DESJ0342-5355A	8	ACT, RedM	4.47 ± 0.52	(B), (D)
DESJ0342-5355B	8	ACT, RedM	11.24 ± 0.46	(B), (D)
DESJ0342-2342	5	RNA	5.51 ± 0.72	…
DESJ0345-3403	4	ACT, RedM	9.82 ± 3.65	…
DESJ0348-2145	9	RNA, ACT, RedM, SPTPol	8.72 ± 0.83	SPT-CL J0348-2144 (m), (D)
DESJ0352-3825	8	RedM	3.18 ± 0.43	DES J035242-382544 (A), (D)
DESJ0354-4446	7	RNA, TI, RedM	3.81 ± 0.46	(B)
DESJ0356-5607	5	RedM	3.92 ± 0.44	(D)
DESJ0356-2408	7	RedM	4.97 ± 2.40	DES J035649-240841 (A), (D)

Table 3
(Continued)

System Name	Rank	Algorithm	θ_E ($''$)	References
DESJ0357-4756	10	RedM	8.63 ± 1.30	(B)
DESJ0358-2415	3	RNA, RNA2, ACT	13.05 ± 1.21	…
DESJ0359-2433	5	RNA, ACT, RedM	10.29 ± 1.06	…
DESJ0402-2205	9	RNA, RedM	5.10 ± 0.57	DESI-060.5238-22.0990 (z), (A), (D)
DESJ0403-5057	6	RNA, RedM	4.16 ± 0.47	(B)
DESJ0406-2254	6	RNA	4.94 ± 0.60	DESI-061.5534-22.9034 (z)
DESJ0411-4506	3	RNA, RedM	4.21 ± 0.50	(B)
DESJ0411-4819	9	RNA, ACT, RedM	7.08 ± 0.54	SPT-CL J0411-4819 (p), (B), (D)
DESJ0413-1958	6	RNA	3.32 ± 0.33	…
DESJ0413-5117	7	ACT	2.79 ± 0.38	…
DESJ0415-4143	7	ACT	6.72 ± 0.27	(C), (D)
DESJ0416-2404	3	RNA, ACT, SPTPol, RedM missed	5.58 ± 0.62	MACS J0416.1-2403 (j)
DESJ0416-5525	7	RNA, RedM	4.34 ± 0.51	(B), (D)
DESJ0422-2803	8	RNA	2.53 ± 0.36	DESI-065.6447-28.0652 (z), (A)
DESJ0424-3317	9	RNA, RedM, BBNA	5.49 ± 0.29	(D)
DESJ0438-3220	4	RNA, ACT, RedM	4.84 ± 0.55	DESI-069.5641-32.3475 (z)
DESJ0440-2658	6	RNA, RedM	10.55 ± 1.37	DESI-070.1928-26.9754 (z)
DESJ0440-4657	6	RNA, ACT, RedM	8.36 ± 0.88	(B)
DESJ0448-3019	6	ACT, RedM, SPTPol	13.98 ± 0.41	DESI-072.0528-30.3308 (z)
DESJ0451-1856	3	RNA, ACT, RedM	21.89 ± 2.20	…
DESJ0453-4120	3	RedM	2.22 ± 0.34	…
DESJ0453-3639	3	RedM	3.26 ± 0.42	…
DESJ0455-2530	8	RNA, RedM	16.07 ± 0.49	DESI-073.9030-25.5129 (z), (D)
DESJ0459-3756	5	RNA, RedM missed	9.18 ± 0.96	…
DESJ0501-2425	8	RNA, RedM	27.39 ± 2.75	DESI-075.2790-24.4179 (z)
DESJ0509-5342	6	ACT, RedM	9.52 ± 0.88	(B), (D)
DESJ0510-3232	7	RedM	3.90 ± 0.33	(D)
DESJ0512-3847	8	RNA, SPTPol, RedM missed	28.82 ± 4.04	SPT-CL J0512-3848 (m), (D)
DESJ0513-2128	5	RNA, RedM missed	5.39 ± 0.60	DESI-078.3580-21.4717 (z), (D)
DESJ0513-3050	9	RedM	6.11 ± 0.54	DESI-078.3561-30.8433 (z)
DESJ0514-5142	5	RNA, RedM	5.26 ± 0.59	(B)
DESJ0516-2208	4	RNA, RedM	2.39 ± 0.36	DES J051603-220847 (A), (D)
DESJ0517-2526	5	RedM	5.77 ± 0.63	…
DESJ0518-4348	6	BNA	3.76 ± 0.46	…
DESJ0524-2721	6	RedM	6.56 ± 0.47	(D)
DESJ0525-4424	8	RNA	3.38 ± 0.43	(B), (D)
DESJ0525-3712	5	RedM	5.56 ± 0.61	…
DESJ0527-1858	7	RedM	6.79 ± 1.45	DESI-081.7547-18.9674 (z)
DESJ0528-2633	6	RNA	4.69 ± 0.89	DESI-082.1548-26.5667 (z)
DESJ0528-3958	6	RNA	5.31 ± 0.93	…
DESJ0531-3158	5	RedM	5.33 ± 0.59	(D)
DESJ0540-2127	8	RNA, ACT, RedM, SPTPol	14.37 ± 0.38	SPT-CL J0540-2127 (m)
DESJ0545-2635	8	RNA, BBNA	13.37 ± 0.29	DESI-086.3066-26.5884 (z)
DESJ0548-3614	7	RedM	7.09 ± 0.76	DESI-087.1525-36.2427 (z)
DESJ0553-3342	6	RNA, ACT, SPTPol	11.41 ± 2.17	SPT-CL J0553-3342 (m), (r)
DESJ0557-4113	6	ACT	15.77 ± 1.60	(B)
DESJ0603-3558	9	ACT	16.35 ± 0.95	DESI-090.9854-35.9683 (z)
DESJ0604-3347	5	RNA, RedM	7.86 ± 0.83	…
DESJ0610-5559A	8	RedM	4.06 ± 0.48	(B)
DESJ0610-5559B	8	RedM	9.22 ± 0.37	(B)
DESJ0611-5514A	9	RNA, RedM	9.26 ± 1.42	(B)
DESJ0611-5514B	9	RNA, RedM	8.06 ± 1.38	(B)
DESJ0612-3920	3	RNA, ACT, RedM	3.59 ± 0.44	(D)
DESJ2011-5228	10	RNA, ACT	13.04 ± 4.23	SPT-CL J2011-5228 (q), (B)
DESJ2011-5725	3	ACT, BBNA	13.62 ± 1.39	…
DESJ2019-5642	6	ACT	17.39 ± 1.76	…
DESJ2022-6032	4	RNA, RedM missed	7.66 ± 0.32	…
DESJ2023-5535	3	ACT, RedM missed	7.44 ± 0.79	…
DESJ2025-5117	4	RNA, ACT	7.29 ± 0.77	(B)
DESJ2028-4316	3	RNA, RedM missed	4.45 ± 0.52	…
DESJ2031-4037	6	ACT	23.88 ± 2.40	SMACS J2031.8-4036 (k)
DESJ2046-6146	3	RNA, RedM missed	6.64 ± 0.71	…
DESJ2106-4411	3	RedM	4.79 ± 1.15	(D)
DESJ2111-0114	9	ACT	10.73 ± 0.60	ClG J2111-0115 (c), (e), (B)
DESJ2112-4801	8	RNA, RedM	6.31 ± 0.68	…
DESJ2122-0059	8	RedM	3.00 ± 0.40	(B)
DESJ2124-6125	9	RNA, RedM	3.70 ± 0.45	…
DESJ2134-4238	3	ACT, RedM missed	31.98 ± 3.21	…
DESJ2138-6007	10	RedM	22.45 ± 7.61	…
DESJ2139-4251	6	RNA, RedM	2.83 ± 0.39	(D)
DESJ2144-4323	3	RedM	7.73 ± 0.82	…
DESJ2145-5644	5	ACT, RedM	28.95 ± 0.66	…

Table 3
(Continued)

System Name	Rank	Algorithm	θ_E ($''$)	References
DESJ2152-5555	6	BBNA	3.21 ± 0.42	…
DESJ2154-4604	6	RedM	3.91 ± 0.47	…
DESJ2157-5700	4	RedM	4.61 ± 0.53	(B)
DESJ2159-6245	6	RNA, RedM missed	5.90 ± 0.65	…
DESJ2200-4128	6	ACT, RedM	1.98 ± 0.33	(D)
DESJ2201-5956	3	ACT, BBNA	19.18 ± 1.94	…
DESJ2208-0124	4	BNA	3.02 ± 0.40	(B)
DESJ2219-4348	7	RedM	3.15 ± 0.36	DES J221912-434835 (A), (D)
DESJ2223-6329	7	RedM	4.83 ± 0.62	…
DESJ2232-5959	4	RNA, ACT	8.56 ± 0.37	(D)
DESJ2232-5807	7	RedM	8.11 ± 0.85	(B)
DESJ2233-0104	4	ACT	5.12 ± 0.48	HSCJ223316-010409 (w)
DESJ2240-5245	5	ACT, RedM	6.17 ± 0.67	(B)
DESJ2248-4431	7	RNA, ACT	32.51 ± 0.40	AS1063 (n), (B), (D)
DESJ2254-4620	5	ACT, RedM missed	33.45 ± 3.26	(B)
DESJ2300-5820	5	RNA, RedM missed	8.06 ± 0.35	(B)
DESJ2308-0211	7	RNA, RedM	35.98 ± 3.61	A2537 (s), (z), (D)
DESJ2311-6307	5	BNA	2.86 ± 0.39	…
DESJ2321-4630	9	BNA	3.13 ± 0.32	DES J232128-463049 (A), (B), (D)
DESJ2322-6409	9	RedM	9.19 ± 0.58	(D)
DESJ2324-4944	7	RedM	5.08 ± 0.29	(B)
DESJ2325-4111	7	ACT, RedM	42.37 ± 0.33	(B), (D)
DESJ2331-5051	7	ACT	16.84 ± 0.30	…
DESJ2332-0152	5	BNA	3.40 ± 0.90	…
DESJ2335-4209	5	RedM	4.25 ± 0.50	…
DESJ2335-5152	7	RNA, RedM	3.64 ± 0.50	DES J233551-515217 (A), (B), (D)
DESJ2336-5352	7	ACT, RedM	6.33 ± 2.03	DES J2336-5352 (o), (B), (D)
DESJ2341-5716	7	RedM	8.55 ± 0.29	DESI-355.2727-57.2679 (z)
DESJ2342-4652	5	RedM	7.27 ± 0.77	…
DESJ2343-6039	6	RedM	11.11 ± 1.14	…
DESJ2347-6246	7	RedM	6.30 ± 0.68	DESI-356.7894-62.7765 (z)
DESJ2347-6245	3	RedM	10.34 ± 1.07	…
DESJ2349-5113	9	RNA, RedM	4.51 ± 0.70	DES J234930-511339 (A), (B), (D)
DESJ2351-5452	10	RNA, ACT, RedM	7.43 ± 1.20	Elliot Arc (f), (B), (D)
DESJ2358-6125	8	RedM	4.82 ± 0.55	DESI-359.7003-61.4330 (z)
DESJ2359+0208	9	RNA, ACT, RedM	8.88 ± 0.80	DESI-359.8897+02.1399 (v), (w)

Note. Properties of all systems presented in this work. Names: algorithms that detected the system, the visual inspection rank, average radius, and references to detections in other papers. Systems labeled "RedM missed" were not identified in the RedM search, but were later found to match redMaPPer galaxy clusters. The algorithms are as follows: BNA = Blue Near Anything, BBNA = secondary Bright Blue Near Anything search, RNA = Red Near Anything, TI = Tile Inspection, ACT = Atacama Cosmology Telescope cluster sample, RedM = redMaPPer year 3 cluster sample, and SPTPol = SPTPol Extended Cluster Survey clusters.
References. Names are only given for the earliest discovery. Names from Diehl et al. (2017) and Jacobs et al. (2019a, 2019b) are identical to the present work. (a) Cabanac et al. (2007), (b) Estrada et al. (2007), (c) Hennawi et al. (2008), (d) Wuyts et al. (2010), (e) Bayliss et al. (2011), (f) Buckley-Geer et al. (2011), (g) Bayliss (2012), (h) Furlanetto et al. (2013b), (i) Stark et al. (2013), (j) Jauzac et al. (2014), (k) Richard et al. (2015), (l) Zitrin et al. (2015), (m) Bleem et al. (2015), (n) Caminha et al. (2016), (o) Nord et al. (2016), (p) Bayliss et al. (2016), (q) Collett et al. (2017), (r) Ebeling et al. (2017), (s) Cerny et al. (2018), (t) Diego et al. (2018), (u) Petrillo et al. (2019), (v) Huang et al. (2020), (w) Jaelani et al. (2020), (x) Li et al. (2020), (y) Cañameras et al. (2020), (z) Huang et al. (2021), (A) Rojas et al. (2021), (B) Diehl et al. (2017), (C) Jacobs et al. (2019a), and (D) Jacobs et al. (2019b).

(This table is available in machine-readable form.)

redshift than their respective lenses. For some systems, this discrepancy is likely due to catastrophic redshift errors in the blue source objects, as mentioned in Section 2.

Table 3 provides an overview of each candidate lens system, including: the system name, algorithms or catalogs that identified the candidates for scanning, system rank, Einstein radius estimate (described below), and references to previous discoveries of the system. Figures 10 through 17 show three-color cutouts of each system. The cutouts are made from the DES Y6A1 coadded tiles using the *i*-, *r*-, and *g*-bands for the red–green–blue color channels, respectively. Where SL systems fell across tile edges, multiple coadd tiles were stitched together to form one cutout. Each cutout was dynamically scaled to fit the system well within the cutout based on the radial distance from the lens center to the furthest lensed source image.

Each image is centered on the most likely lens galaxy, labeled by the letter "A." For systems where the primary lens was uncertain, or where sources were clearly perturbed by multiple galaxies, additional lens galaxies are marked with roman letters "B," "C," etc. All lenses are found in the DESDM Y3 or Y6 catalogs. Source objects that were identified in DESDM are labeled by number, e.g., "1," "2," etc. Source objects that were not identified in DESDM had their positions determined manually, and are shown by an arrow.

To identify positions and photometry for lens and source objects, the DES Y3 and Y6 catalogs were overlaid on images of candidates in the Target Viewer. Lens and source images

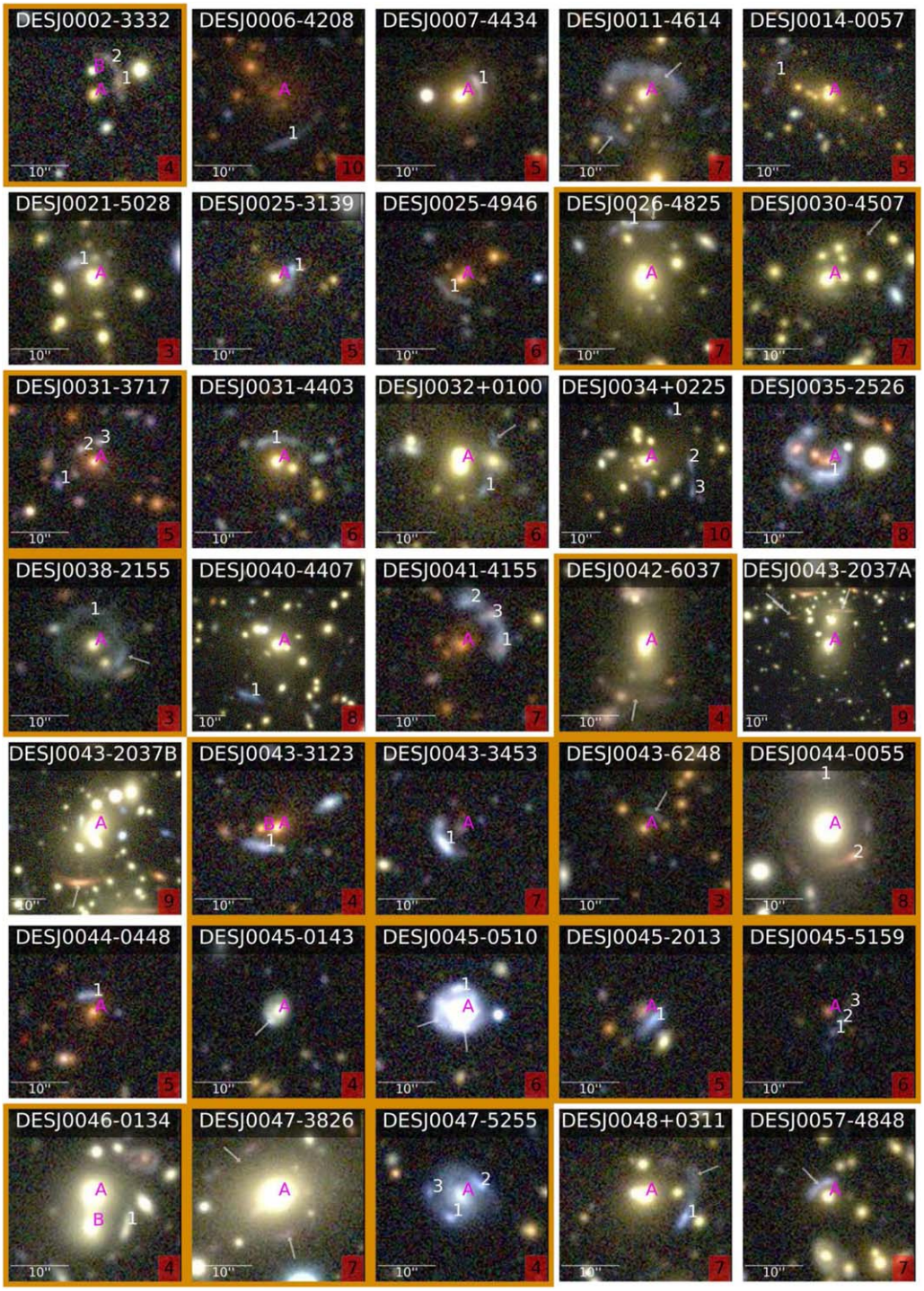

Figure 10. First page of SL systems with a rank of 3 or more. Each cutout image has the visual inspection ranking displayed in a red box in the lower right corner. All images are oriented with north being the top, and east to the left. Each cutout is dynamically sized to fit the SL system well within the cutout, with a minimum size of $30'' \times 30''$. A $10''$ long scale bar is displayed in the lower left corner. New SL systems are outlined with a gold border, previously known systems with white.

were matched to the catalog object IDs. Y6 object identifications were preferred over Y3; however, in cases where an object was not detected in Y6, or was blended with another object, the object was matched to the Y3 catalog. Within each system, catalogs were kept consistent, such that no system mixes Y3 data for some objects with Y6 data for others. Some source images could not be accurately associated with a known DES object, and their position was estimated manually. Table 4 shows the positions and photometry for all systems presented in this paper.

We identified those systems presented here that were previously known, as well as those that are new. To do so, we checked the candidates against the Master Lens Database (Moustakas et al. 2012), the list of objects labeled as strong-lens candidates or known systems in SIMBAD (Wenger et al. 2000), and other SL search papers. Previous discoveries of all

Table 4
Names, Positions, Photometry, and Photometric Redshifts of Objects for Each Candidate Lensing System

System Name (Object Label)	R.A. (J2000)	Decl. (J2000)	Magnitudes (g, r, i, z, Y)	$z_{\rm photo}$
DESJ0002-3332 (A)	0.527213	−33.544062	(22.67 ± 0.08, 21.00 ± 0.02, 20.35 ± 0.02, 20.02 ± 0.04, 19.92 ± 0.08)	0.50 ± 0.03
DESJ0002-3332 (B)	0.527307	−33.542925	(22.45 ± 0.05, 21.12 ± 0.02, 20.70 ± 0.02, 20.45 ± 0.04, 20.44 ± 0.11)	0.48 ± 0.08
DESJ0002-3332 (1)	0.525724	−33.543500	(22.12 ± 0.07, 21.05 ± 0.04, 20.50 ± 0.04, 20.27 ± 0.07, 20.54 ± 0.23)	0.68 ± 0.05
DESJ0002-3332 (2)	0.526278	−33.542441	(22.57 ± 0.09, 21.64 ± 0.05, 21.15 ± 0.05, 21.12 ± 0.13, 21.42 ± 0.40)	0.67 ± 0.06
DESJ0007-4434 (A)	1.872055	−44.579515	(20.42 ± 0.01, 18.73 ± 0.00, 18.01 ± 0.00, 17.62 ± 0.01, 17.45 ± 0.01)	0.51 ± 0.01
DESJ0007-4434 (1)	1.870997	−44.578933	(21.74 ± 0.01, 21.01 ± 0.01, 20.42 ± 0.01, 20.08 ± 0.01, 19.95 ± 0.03)	0.73 ± 0.09
DESJ0011-4614 (A)	2.971390	−46.239450	(20.18 ± 0.01, 19.14 ± 0.00, 18.46 ± 0.00, 18.00 ± 0.01, 17.84 ± 0.01)*	0.57 ± 0.02*
DESJ0011-4614 (1)	2.970150	−46.238660	…	…
DESJ0011-4614 (2)	2.973640	−46.241360	…	…
DESJ0014-0057 (A)	3.725464	−0.952317	(21.14 ± 0.03, 19.24 ± 0.01, 18.45 ± 0.01, 18.04 ± 0.01, 17.94 ± 0.02)	0.53 ± 0.00
DESJ0014-0057 (1)	3.728786	−0.951020	(21.25 ± 0.06, 20.28 ± 0.04, 19.64 ± 0.03, 19.41 ± 0.05, 19.35 ± 0.16)*	0.54 ± 0.19*
DESJ0021-5028 (A)	5.452849	−50.476040	(20.37 ± 0.01, 18.80 ± 0.00, 18.26 ± 0.00, 17.94 ± 0.01, 17.81 ± 0.02)	0.37 ± 0.02
DESJ0021-5028 (1)	5.454124	−50.475333	(21.65 ± 0.01, 20.94 ± 0.01, 20.63 ± 0.02, 20.37 ± 0.02, 20.34 ± 0.08)	0.20 ± 0.06
DESJ0025-3139 (A)	6.292237	−31.657593	(21.38 ± 0.05, 19.88 ± 0.02, 19.15 ± 0.02, 18.81 ± 0.02, 18.57 ± 0.04)*	0.56 ± 0.03*
DESJ0025-3139 (1)	6.291383	−31.657199	(22.09 ± 0.03, 21.46 ± 0.03, 21.04 ± 0.03, 20.78 ± 0.04, 20.70 ± 0.10)	0.22 ± 0.15
DESJ0025-4946 (A)	6.294487	−49.774042	(22.23 ± 0.06, 20.66 ± 0.02, 19.58 ± 0.01, 19.19 ± 0.02, 19.04 ± 0.04)*	0.69 ± 0.04*
DESJ0025-4946 (1)	6.295470	−49.774668	(22.42 ± 0.06, 21.61 ± 0.04, 21.03 ± 0.04, 20.70 ± 0.06, 21.08 ± 0.24)	0.75 ± 0.06
DESJ0026-4825 (A)	7.049739	−48.435200	(19.37 ± 0.01, 17.60 ± 0.00, 17.03 ± 0.00, 16.71 ± 0.00, 16.57 ± 0.01)*	0.38 ± 0.01*
DESJ0026-4825 (1)	7.051111	−48.432314	(21.62 ± 0.02, 20.57 ± 0.01, 20.16 ± 0.01, 19.82 ± 0.02, 19.67 ± 0.04)	0.45 ± 0.13
DESJ0026-4825 (2)	7.049190	−48.432200	…	…
DESJ0030-4507 (A)	7.663571	−45.117814	(20.88 ± 0.01, 19.19 ± 0.00, 18.62 ± 0.00, 18.28 ± 0.01, 18.17 ± 0.02)	0.40 ± 0.04
DESJ0030-4507 (1)	7.661060	−45.115780	…	…
DESJ0031-3717 (A)	7.779623	−37.292908	(22.28 ± 0.06, 20.66 ± 0.02, 19.56 ± 0.01, 19.05 ± 0.01, 18.89 ± 0.03)	0.74 ± 0.03
DESJ0031-3717 (1)	7.781746	−37.293924	(22.84 ± 0.07, 22.47 ± 0.07, 22.18 ± 0.09, 21.91 ± 0.13, 21.35 ± 0.25)	0.90 ± 0.35
DESJ0031-3717 (2)	7.780348	−37.292305	(23.27 ± 0.05, 22.28 ± 0.03, 21.67 ± 0.03, 21.37 ± 0.03, 21.28 ± 0.10)	0.62 ± 0.11
DESJ0031-3717 (3)	7.779335	−37.291970	(22.72 ± 0.06, 21.92 ± 0.04, 21.51 ± 0.05, 21.12 ± 0.06, 20.86 ± 0.16)	0.42 ± 0.12
DESJ0032+0100 (A)	8.073145	1.010437	(20.08 ± 0.02, 18.28 ± 0.00, 17.67 ± 0.00, 17.33 ± 0.00, 17.18 ± 0.01)†	0.39 ± 0.00†
DESJ0032+0100 (1)	8.072042	1.009085	(22.30 ± 0.06, 21.16 ± 0.03, 20.62 ± 0.03, 20.41 ± 0.04, 20.33 ± 0.14)†	0.23 ± 0.06†
DESJ0032+0100 (2)	8.071510	1.011570	…	…
DESJ0034+0225 (A)	8.617365	2.422945	(20.16 ± 0.01, 18.46 ± 0.00, 17.88 ± 0.00, 17.57 ± 0.00, 17.50 ± 0.01)*	0.38 ± 0.03*
DESJ0034+0225 (1)	8.615521	2.426298	(23.09 ± 0.32, 20.59 ± 0.04, 20.27 ± 0.06, 20.65 ± 0.17, 99.00 ± 99.00)	0.66 ± 0.71
DESJ0034+0225 (2)	8.614283	2.422975	(21.93 ± 0.06, 20.79 ± 0.03, 20.45 ± 0.04, 20.41 ± 0.08, 20.48 ± 0.24)*	0.21 ± 0.18*
DESJ0034+0225 (3)	8.613881	2.420758	(22.11 ± 0.05, 21.66 ± 0.05, 21.59 ± 0.08, 21.57 ± 0.17, 22.62 ± 1.32)	0.72 ± 0.67
DESJ0035-2526 (A)	8.779998	−25.449930	(22.47 ± 0.03, 21.41 ± 0.01, 20.49 ± 0.01, 20.00 ± 0.01, 19.87 ± 0.04)*	0.64 ± 0.51*
DESJ0035-2526 (1)	8.780002	−25.450581	(20.54 ± 0.01, 20.03 ± 0.01, 19.85 ± 0.01, 19.68 ± 0.02, 19.47 ± 0.05)	0.05 ± 0.05
DESJ0038-2155 (A)	9.716928	−21.924359	(21.15 ± 0.02, 19.84 ± 0.01, 19.42 ± 0.01, 19.15 ± 0.01, 18.99 ± 0.03)	0.39 ± 0.05
DESJ0038-2155 (1)	9.717215	−21.922871	(22.42 ± 0.07, 21.47 ± 0.04, 21.35 ± 0.06, 21.13 ± 0.09, 21.07 ± 0.27)*	0.11 ± 0.00*
DESJ0038-2155 (2)	9.715270	−21.924870	…	…

Note. Only the first 13 systems are shown; data for all systems is available in machine-readable format. Objects that did not have a corresponding detection in DES Y3 or DES Y6 data have no photometry or photometric redshift are represented as ellipses (…). Photometry and photometric redshifts with (without) a dagger (†) are derived from the DES Y3 (DES Y6) data. Photometry and photometric redshifts marked with (∗) have `FLAGS_GOLD` ! = 0, indicating a likely problem with the object's identification or photometry.

(This table is available in its entirety in machine-readable form.)

systems are given in Table 3. Note that references include both confirmed and candidate strong-lens systems, i.e., systems with external references are not guaranteed to be true lenses. We include these previously discovered systems in this work because we provide the positions, photometry, and photometric redshifts of system components (see Table 4), as well as an estimate of the Einstein radius (see Table 3), forming a standardized data set which may be of use in further studies.

The average radius of the source images is an approximation for the Einstein radius, and is identical to that when the true source position is directly behind the lens. We estimate the Einstein radius from the mean separation between the primary lens and each source image. For systems with multiple source images, the uncertainty is taken as the standard deviation of these separations. For systems with only one source image, the uncertainty is taken as 10% of the source–lens separation, typical for the scatter of

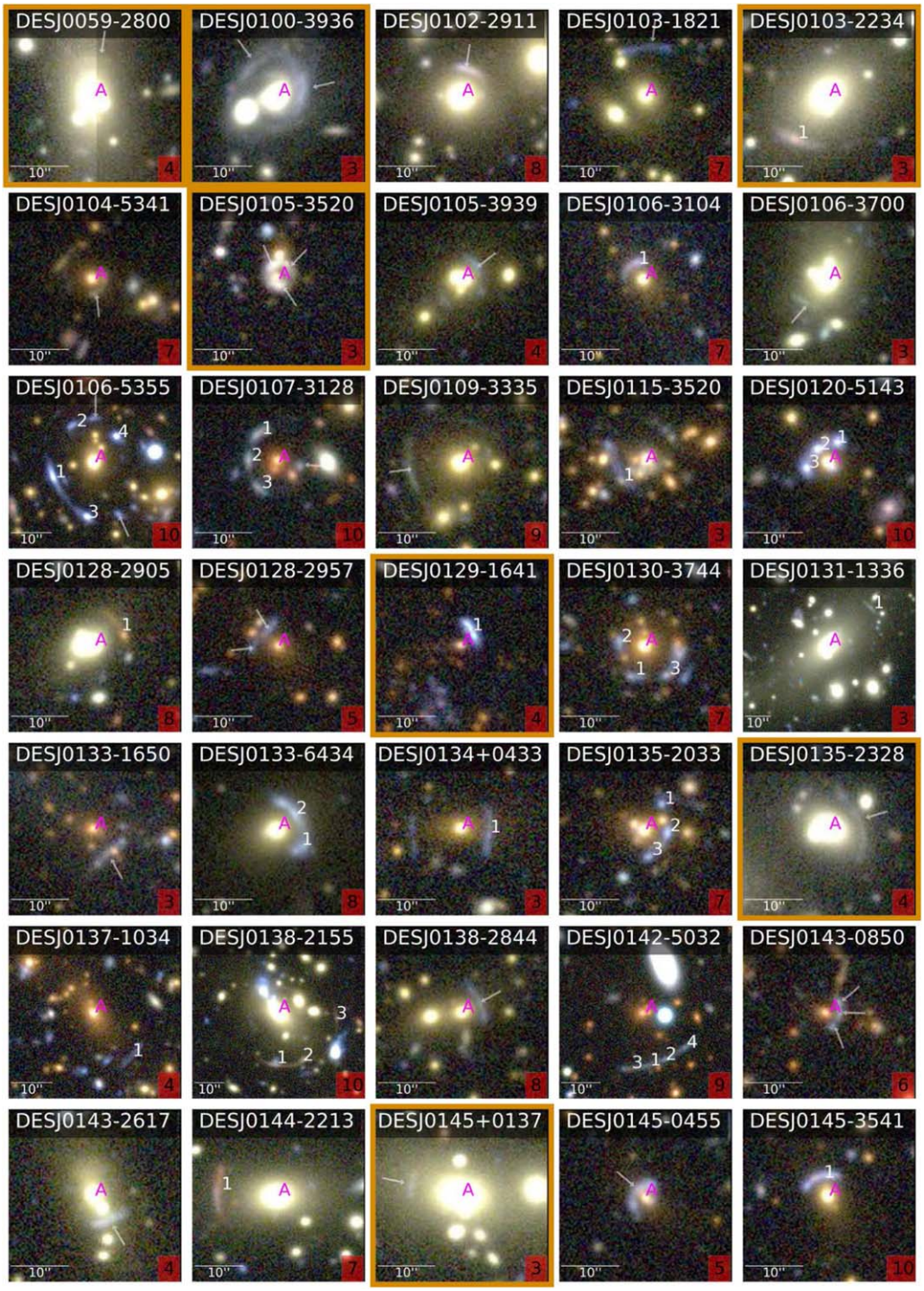

Figure 11. Second page of SL systems with a rank of 3 or more. Each cutout image has the visual inspection ranking displayed in a red box in the lower right corner. All images are oriented with north being the top, and east to the left. Each cutout is dynamically sized to fit the SL system well within the cutout, with a minimum size of 30″ × 30″. A 10″ long scale bar is displayed in the lower left corner. New SL systems are outlined with a gold border, previously known systems with white.

individual sources in systems with multiple images. Especially for these systems with a single lensed image, this tends to provide an overestimate of the Einstein radius (Kneib & Natarajan 2011). In all cases, the uncertainty is summed in quadrature with the DES plate scale of 0.″263 per pixel. The image separation distribution is sensitive to a number of inputs such as the halo mass, the lens mass distribution, and the source redshift. It therefore contains information about the cosmological parameters and various scaling relations between galaxy properties and halo mass, and can be measured from galaxy to cluster scales (Oguri 2006; More et al. 2016). A similar metric has been found to be an effective measure for the inner halo mass by Remolina González et al. (2020).

4.1. Notable Systems

Here we highlight some notable systems. The newly identified system DESJ2138-6007 is particularly spectacular. It contains a long blue arc with a radius of nearly 30″ and

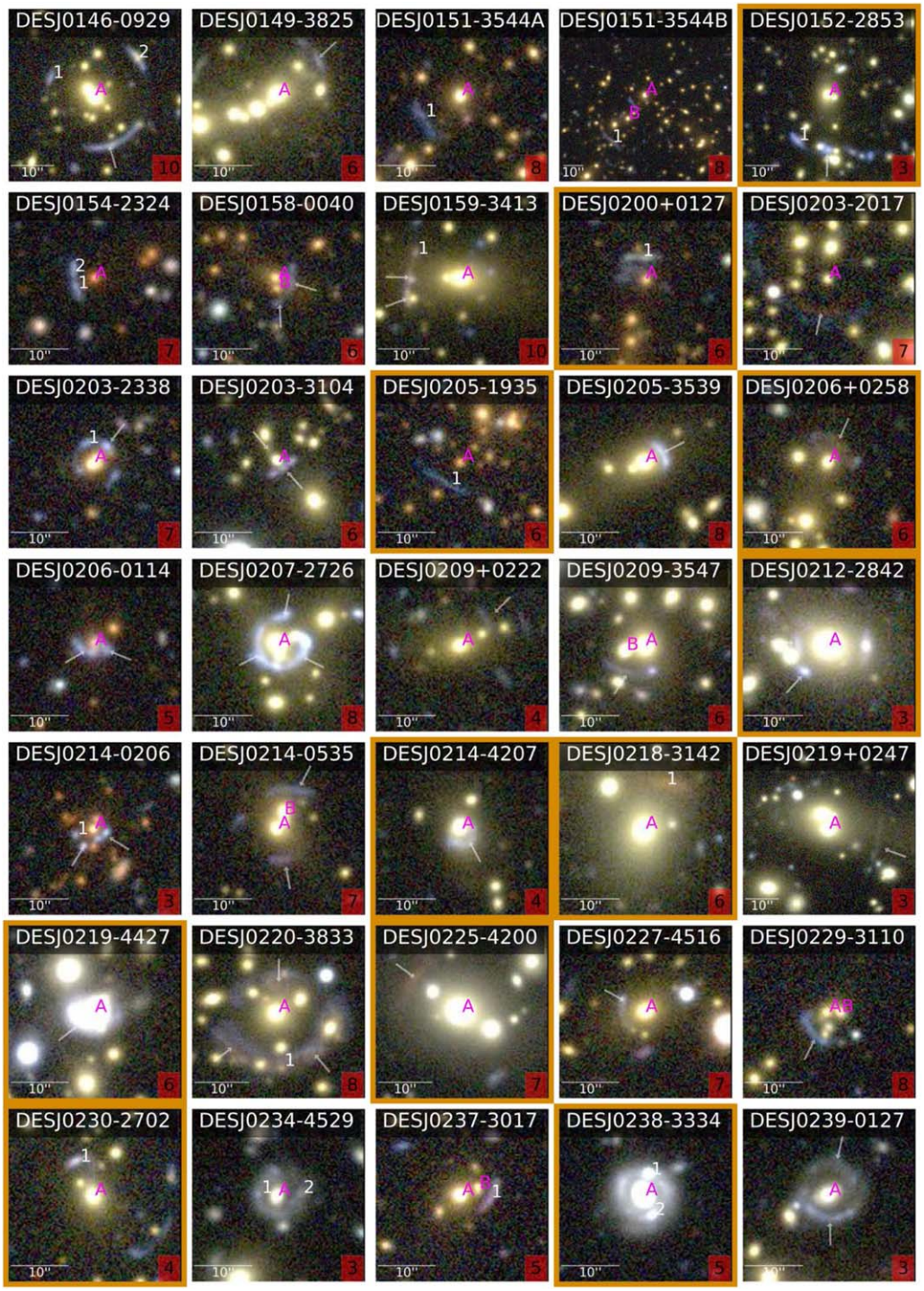

Figure 12. Third page of SL systems with a rank of 3 or more. Each cutout image has the visual inspection ranking displayed in a red box in the lower right corner. All images are oriented with north being the top, and east to the left. Each cutout is dynamically sized to fit the SL system well within the cutout, with a minimum size of $30'' \times 30''$. A $10''$ long scale bar is displayed in the lower left corner. New SL systems are outlined with a gold border, previously known systems with white.

several possible counterimages. The system is centered on a redMaPPer Y3 galaxy cluster with a richness of 152 ± 5. Four SL systems appear to contain two sources, one red and one blue. In each case the system is listed twice in Tables 3 and 4, with suffixes "A" and "B" for the two distinct sources. These systems are DESJ0151-3544, DESJ0342-5355, DESJ0610-5559, and DESJ0611-5514, which have Y3 redMaPPer richnesses of 73 ± 3, 109 ± 4, 48 ± 4, and 44 ± 4, respectively. System DESJ0151-3544 was previously discovered in SPT follow up (Bleem et al. 2015), and systems DESJ0342-5355 and DESJ0610-5559 were identified and noted as double source SL systems in Diehl et al. (2017). The final one, DESJ0611-5514, is new.

System DESJ0043-2037 is a large, unrelaxed, potential merging galaxy cluster that appears to have two red arcs near its center. In this work, it is presented as two systems with suffixes "A" and "B," centered on two separate luminous galaxies. It is a complex system that merits further study.

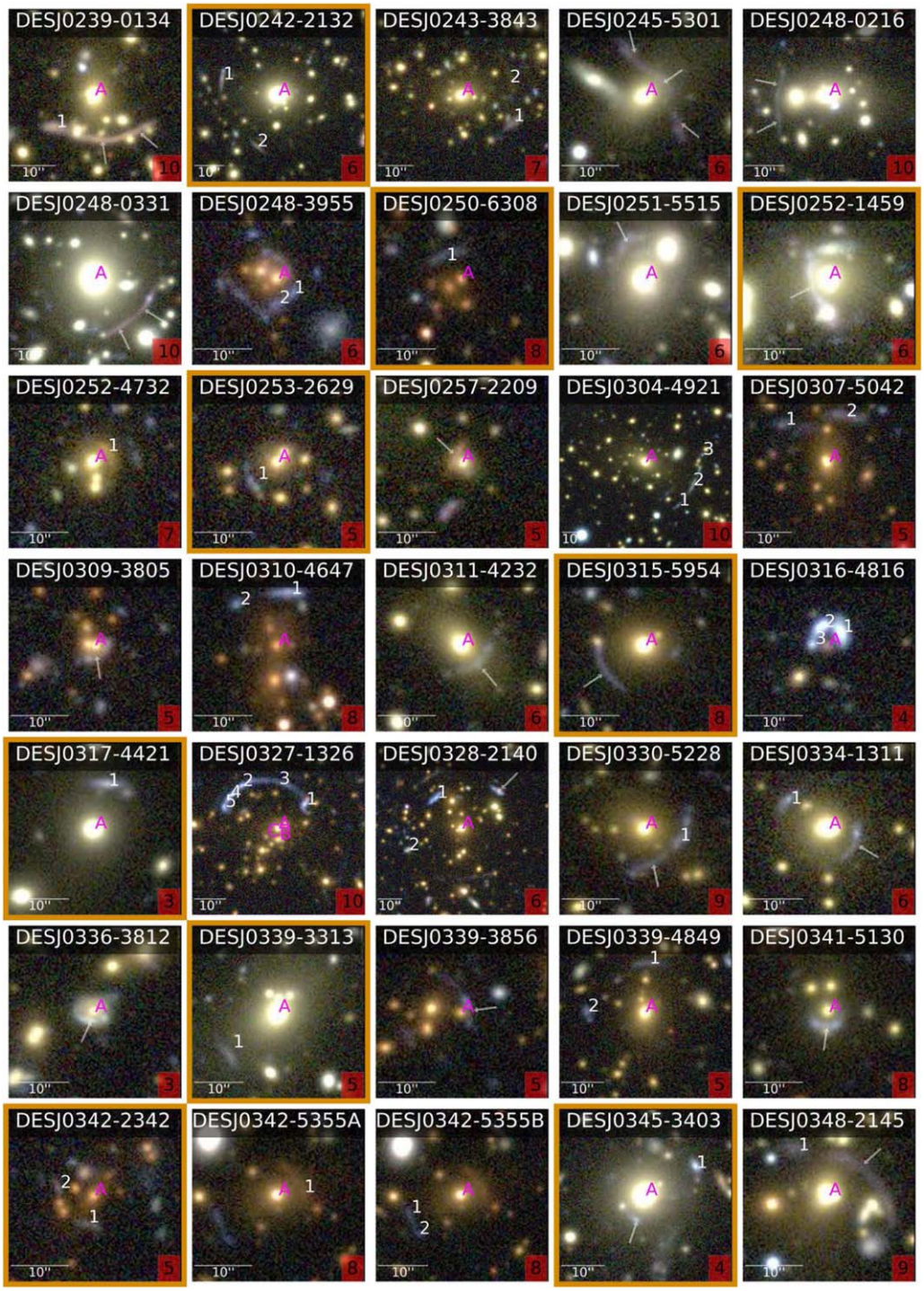

Figure 13. Fourth page of SL systems with a rank of 3 or more. Each cutout image has the visual inspection ranking displayed in a red box in the lower right corner. All images are oriented with north being the top, and east to the left. Each cutout is dynamically sized to fit the SL system well within the cutout, with a minimum size of $30'' \times 30''$. A $10''$ long scale bar is displayed in the lower left corner. New SL systems are outlined with a gold border, previously known systems with white.

Higher resolution imaging of other systems presented here might expose additional remarkable features, such as central images, radial arcs, or substructure lensing in some of these systems. These features would provide significant information about the matter distribution in the lens systems.

5. Summary and Conclusion

We report the results of eight searches for strong gravitational lens candidates in the full 5000 square degree footprint of the DES imaging data. We searched the DES catalogs for spatial matches of potential lens and source candidates using the BNA and RNA algorithms. We searched the positions of known ACT, SPTPol, and DES redMaPPer galaxy clusters. The scanning of wide-area tiles for the DES data-quality effort led to the serendipitous discovery of several SL systems. For all of the searches we produced a short list of candidates and then evaluated cutouts to identify the most promising systems based on

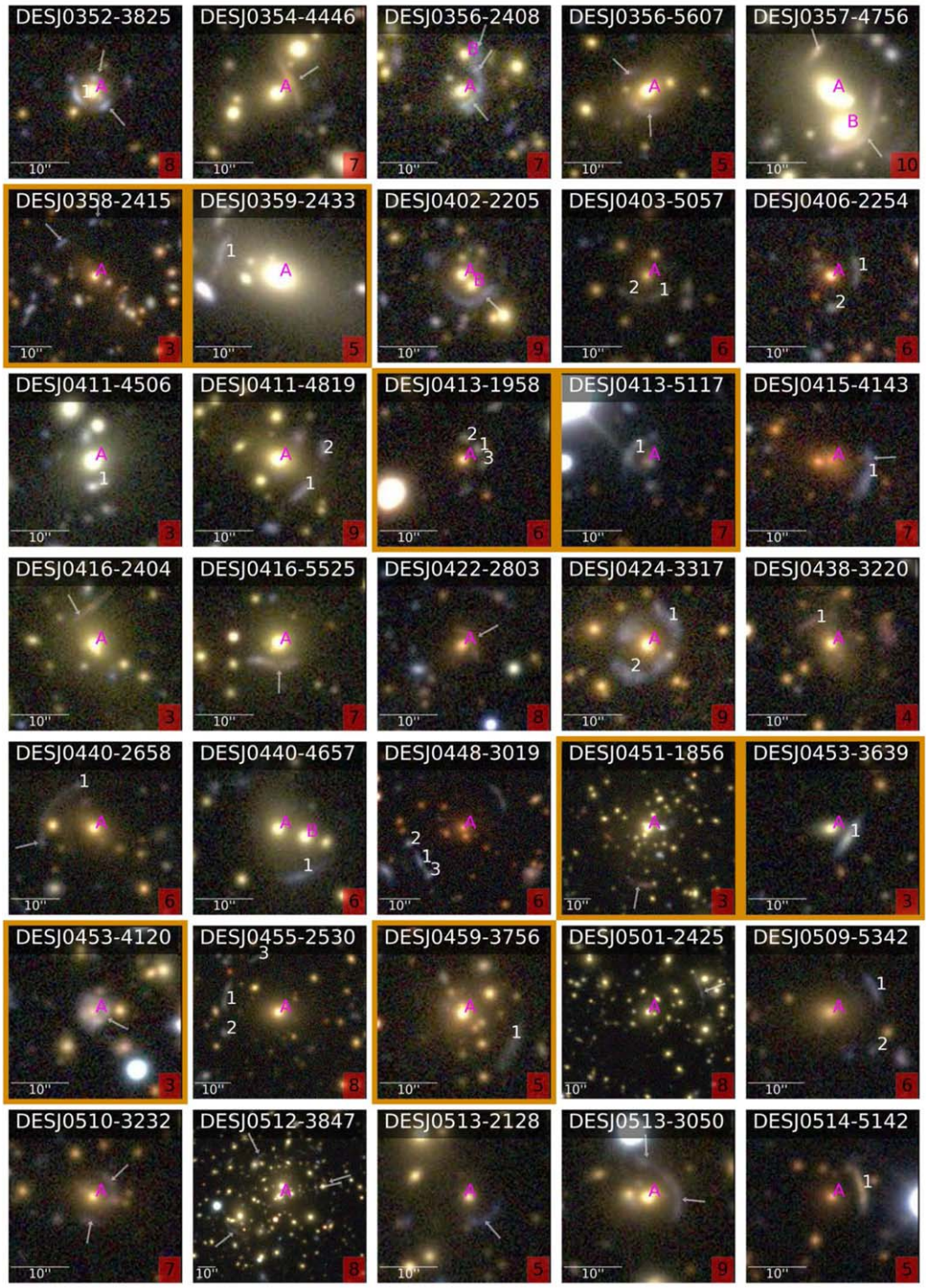

Figure 14. Fifth page of SL systems with a rank of 3 or more. Each cutout image has the visual inspection ranking displayed in a red box in the lower right corner. All images are oriented with north being the top, and east to the left. Each cutout is dynamically sized to fit the SL system well within the cutout, with a minimum size of $30'' \times 30''$. A $10''$ long scale bar is displayed in the lower left corner. New SL systems are outlined with a gold border, previously known systems with white.

color and morphology. We then assigned those a rank that quantifies our confidence that the system is a potential strong gravitational lens. Of the 247 systems that we found, 81 are presented for the first time. Of the newly discovered systems, at least one was uniquely found by each of our searches. For each system we provide the position, the magnitudes, and photometric properties of the lens and source objects, and the distance (radius) of the source(s) from the lens center. Some of these are striking systems with giant arcs. Some have red-colored sources. Four have both blue and red candidate sources at differing distances from the candidate lens.

Each category of the search (RNA, BNA, galaxy cluster, and tile inspection) provided unique newly discovered systems, as shown in Figure 6. These varied search strategies serve as effective complements to each other, and each contributed new systems to the final catalog.

These SL systems tend to be galaxy group and cluster-scale candidates, particularly those from the searches of galaxy clusters described in Section 3.4. Therefore, we expect it will be a useful

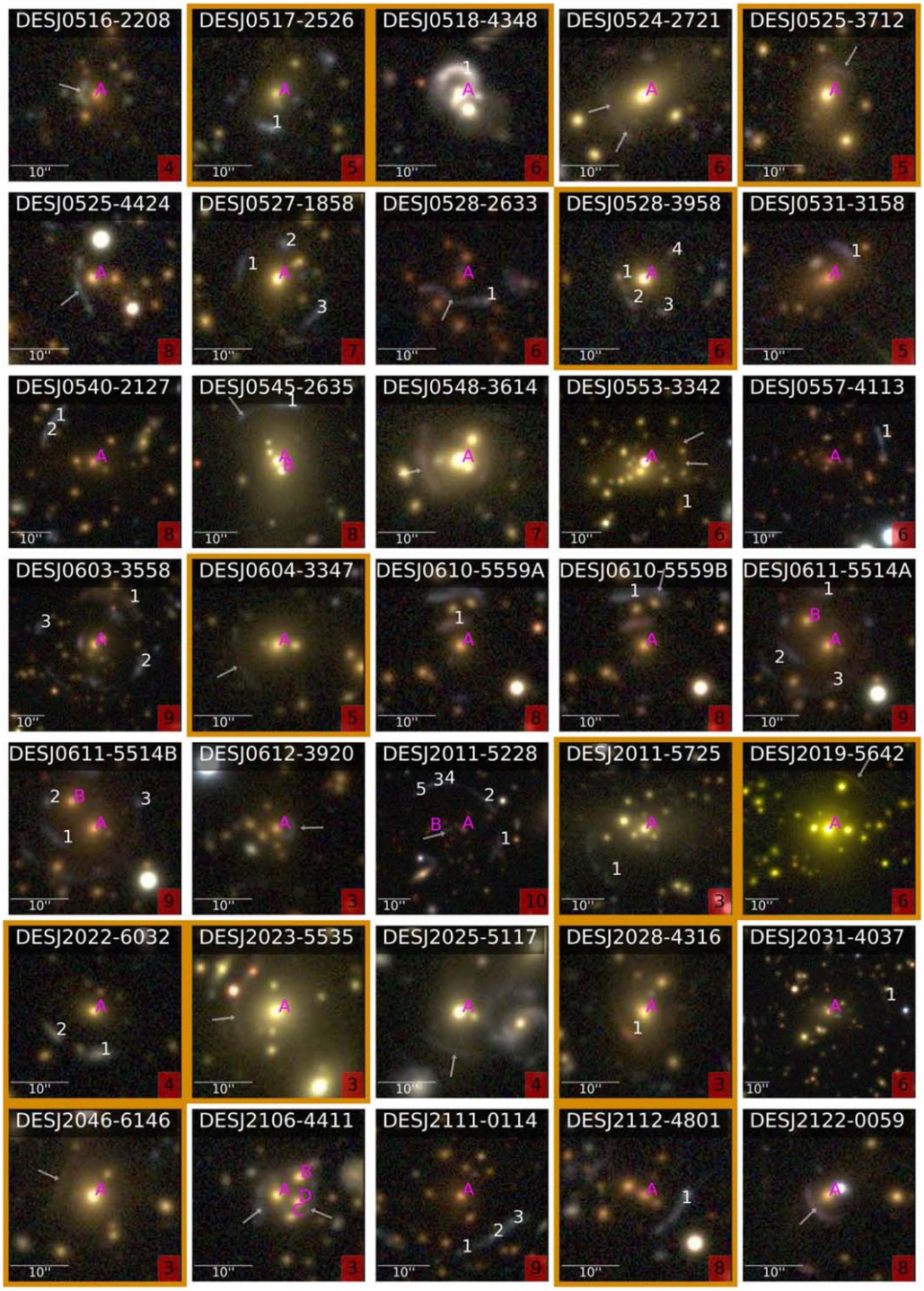

Figure 15. Sixth page of SL systems with a rank of 3 or more. Each cutout image has the visual inspection ranking displayed in a red box in the lower right corner. All images are oriented with north being the top, and east to the left. Each cutout is dynamically sized to fit the SL system well within the cutout, with a minimum size of $30'' \times 30''$. A $10''$ long scale bar is displayed in the lower left corner. New SL systems are outlined with a gold border, previously known systems with white.

and valuable training and validation set for future automated searches of galaxy clusters in new fields and at a lower richness range. At the same time, this catalog also highlights the need for, and importance of, crowdsourced or automated lens modeling techniques (Birrer et al. 2015; Küng et al. 2015) to be developed.[58]

While a majority of the systems discovered in these searches were previously identified (166 of 247), it is clear that many undiscovered systems exist in current data sets. Predictions for the number of lenses in a survey depend on depth and area, but estimates for the full DES range around a few thousand (Oguri & Marshall 2010). In the near future, they are expected to expand to more than 100,000 in Large Synoptic Survey Telescope (LSST) data (Collett 2015). Fortunately, there will be no shortage of high-quality strong-lens systems for follow up and detailed study.

[58] https://github.com/DES-SL/EasyLens and http://linan7788626.github.io/pages/Hoopla/index.html.

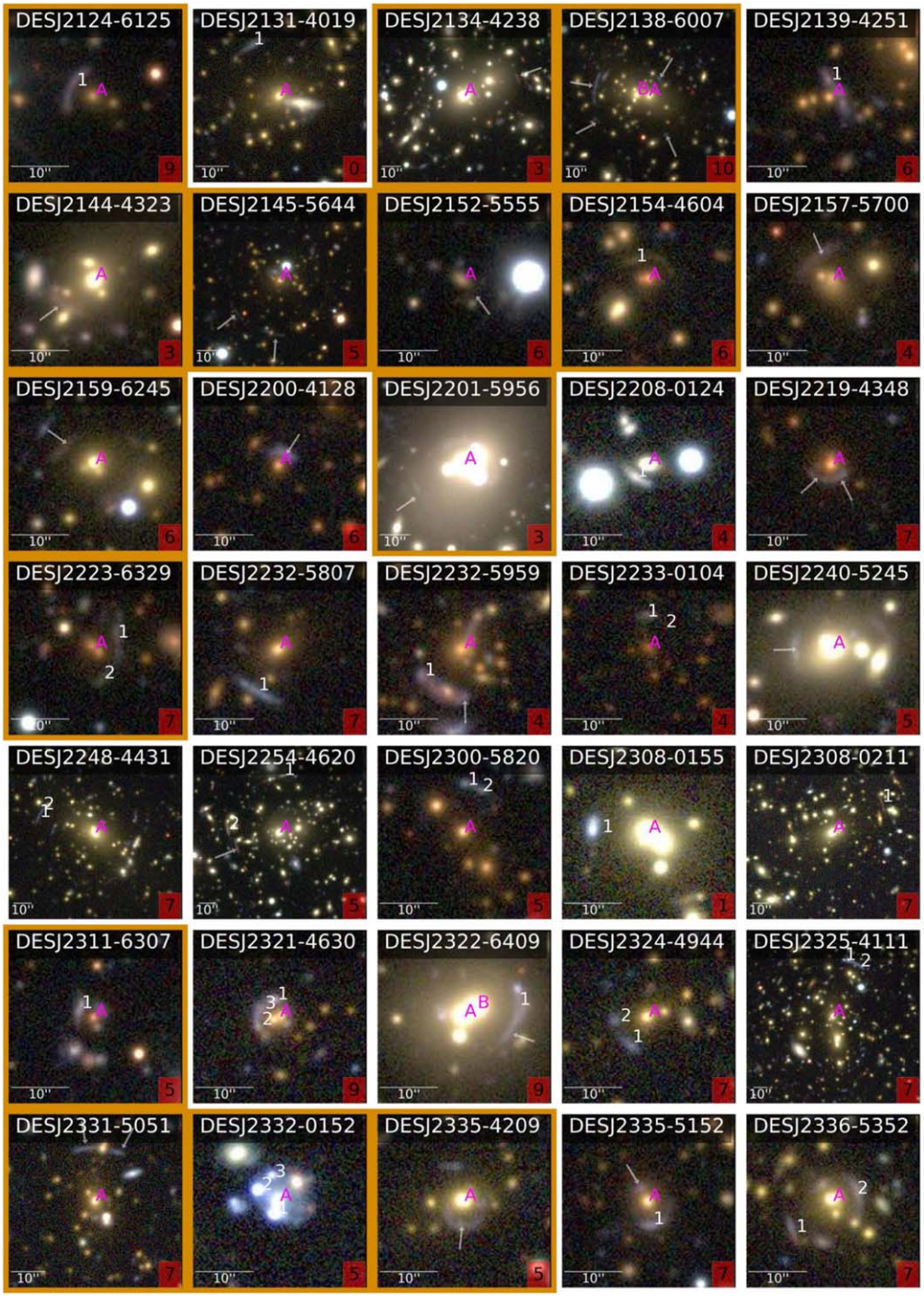

Figure 16. Seventh page of SL systems with a rank of 3 or more. Each cutout image has the visual inspection ranking displayed in a red box in the lower right corner. All images are oriented with north being the top, and east to the left. Each cutout is dynamically sized to fit the SL system well within the cutout, with a minimum size of $30'' \times 30''$. A $10''$ long scale bar is displayed in the lower left corner. New SL systems are outlined with a gold border, previously known systems with white.

This research has made use of the NASA/IPAC Extragalactic Database (NED) which is operated by the California Institute of Technology, under contract with the National Aeronautics and Space Administration.

Some figures in this work were generated with matplotlib (Hunter 2007).

Funding for the DES projects has been provided by the U.S. Department of Energy, the U.S. National Science Foundation, the Ministry of Science and Education of Spain, the Science and Technology Facilities Council of the United Kingdom, the Higher Education Funding Council for England, the National Center for Supercomputing Applications at the University of Illinois at Urbana-Champaign, the Kavli Institute of Cosmological Physics at the University of Chicago, the Center for Cosmology and Astro-Particle Physics at The Ohio State University, the Mitchell Institute for Fundamental Physics and Astronomy at Texas A&M University, Financiadora de Estudos e Projetos, Fundação Carlos Chagas Filho de Amparo

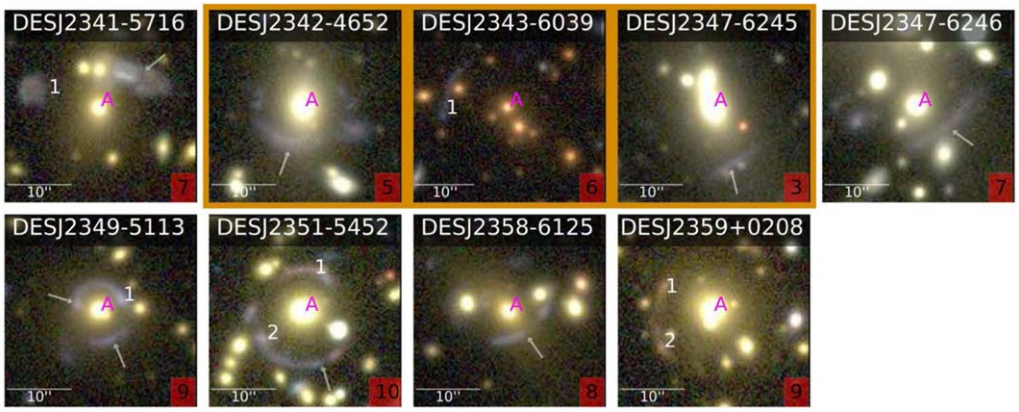

Figure 17. Eighth and last page of SL systems with a rank of 3 or more. Each cutout image has the visual inspection ranking displayed in a red box in the lower right corner. All images are oriented with north being the top, and east to the left. Each cutout is dynamically sized to fit the SL system well within the cutout, with a minimum size of $30'' \times 30''$. A $10''$ long scale bar is displayed in the lower left corner. New SL systems are outlined with a gold border, previously known systems with white.

à Pesquisa do Estado do Rio de Janeiro, Conselho Nacional de Desenvolvimento Científico e Tecnológico and the Ministério da Ciência, Tecnologia e Inovação, the Deutsche Forschungsgemeinschaft, and the Collaborating Institutions in the Dark Energy Survey.

The Collaborating Institutions are Argonne National Laboratory, the University of California at Santa Cruz, the University of Cambridge, Centro de Investigaciones Energéticas, Medioambientales y Tecnológicas-Madrid, the University of Chicago, University College London, the DES-Brazil Consortium, the University of Edinburgh, the Eidgenössische Technische Hochschule (ETH) Zürich, Fermi National Accelerator Laboratory, the University of Illinois at Urbana-Champaign, the Institut de Ciències de l'Espai (IEEC/CSIC), the Institut de Física d'Altes Energies, Lawrence Berkeley National Laboratory, the Ludwig-Maximilians Universität München and the associated Excellence Cluster Universe, the University of Michigan, NSF's NOIRLab, the University of Nottingham, The Ohio State University, the University of Pennsylvania, the University of Portsmouth, SLAC National Accelerator Laboratory, Stanford University, the University of Sussex, Texas A&M University, and the OzDES Membership Consortium.

Based in part on observations at Cerro Tololo Inter-American Observatory at NSF's NOIRLab (NOIRLab Prop. ID 2012B-0001; PI: J. Frieman), which is managed by the Association of Universities for Research in Astronomy (AURA) under a cooperative agreement with the National Science Foundation.

The DES data management system is supported by the National Science Foundation under grant nos. AST-1138766 and AST-1536171. The DES participants from Spanish institutions are partially supported by MICINN under grants ESP2017-89838, PGC2018-094773, PGC2018-102021, SEV-2016-0588, SEV-2016-0597, and MDM-2015-0509, some of which include ERDF funds from the European Union. IFAE is partially funded by the CERCA program of the Generalitat de Catalunya. Research leading to these results has received funding from the European Research Council under the European Union's Seventh Framework Program (FP7/2007-2013) including ERC grant agreements 240672, 291329, and 306478. We acknowledge support from the Brazilian Instituto Nacional de Ciência e Tecnologia (INCT) do e-Universo (CNPq grant 465376/2014-2).

This manuscript has been authored by Fermi Research Alliance, LLC under Contract No. DE-AC02-07CH11359 with the U.S. Department of Energy, Office of Science, Office of High Energy Physics.

ORCID iDs

J. H. O'Donnell https://orcid.org/0000-0003-4083-1530
R. D. Wilkinson https://orcid.org/0000-0002-3908-7313
H. T. Diehl https://orcid.org/0000-0002-8357-7467
C. Aros-Bunster https://orcid.org/0000-0002-9441-3193
S. Birrer https://orcid.org/0000-0003-3195-5507
E. J. Buckley-Geer https://orcid.org/0000-0002-3304-0733
A. Carnero Rosell https://orcid.org/0000-0003-3044-5150
M. Carrasco Kind https://orcid.org/0000-0002-4802-3194
L. N. da Costa https://orcid.org/0000-0002-7731-277X
S. J. Gonzalez Lozano https://orcid.org/0000-0001-7282-3864
R. A. Gruendl https://orcid.org/0000-0002-4588-6517
M. Hilton https://orcid.org/0000-0002-8490-8117
H. Lin https://orcid.org/0000-0002-7825-3206
K. A. Lindgren https://orcid.org/0000-0002-8414-7776
A. Pieres https://orcid.org/0000-0001-9186-6042
E. S. Rykoff https://orcid.org/0000-0001-9376-3135
I. Sevilla-Noarbe https://orcid.org/0000-0002-1831-1953
E. Sheldon https://orcid.org/0000-0001-9194-0441
C. Sifón https://orcid.org/0000-0002-8149-1352
D. L. Tucker https://orcid.org/0000-0001-7211-5729
B. Yanny https://orcid.org/0000-0002-9541-2678
T. M. C. Abbott https://orcid.org/0000-0003-1587-3931
M. Aguena https://orcid.org/0000-0001-5679-6747
J. Annis https://orcid.org/0000-0002-0609-3987
E. Bertin https://orcid.org/0000-0002-3602-3664
D. Brooks https://orcid.org/0000-0002-8458-5047
D. L. Burke https://orcid.org/0000-0003-1866-1950
J. Carretero https://orcid.org/0000-0002-3130-0204
M. Costanzi https://orcid.org/0000-0001-8158-1449
J. De Vicente https://orcid.org/0000-0001-8318-6813
S. Desai https://orcid.org/0000-0002-0466-3288
K. Eckert https://orcid.org/0000-0002-1407-4700
I. Ferrero https://orcid.org/0000-0002-1295-1132
B. Flaugher https://orcid.org/0000-0002-2367-5049
P. Fosalba https://orcid.org/0000-0002-1510-5214

J. Frieman https://orcid.org/0000-0003-4079-3263
J. García-Bellido https://orcid.org/0000-0002-9370-8360
E. Gaztanaga https://orcid.org/0000-0001-9632-0815
D. W. Gerdes https://orcid.org/0000-0001-6942-2736
D. Gruen https://orcid.org/0000-0003-3270-7644
J. Gschwend https://orcid.org/0000-0003-3023-8362
M. S. S. Gill https://orcid.org/0000-0003-2524-5154
G. Gutierrez https://orcid.org/0000-0003-0825-0517
S. R. Hinton https://orcid.org/0000-0003-2071-9349
D. L. Hollowood https://orcid.org/0000-0002-9369-4157
K. Honscheid https://orcid.org/0000-0002-6550-2023
D. J. James https://orcid.org/0000-0001-5160-4486
T. Jeltema https://orcid.org/0000-0001-6089-0365
K. Kuehn https://orcid.org/0000-0003-0120-0808
O. Lahav https://orcid.org/0000-0002-1134-9035
M. Lima https://orcid.org/0000-0002-4719-3781
M. A. G. Maia https://orcid.org/0000-0001-9856-9307
J. L. Marshall https://orcid.org/0000-0003-0710-9474
P. Melchior https://orcid.org/0000-0002-8873-5065
F. Menanteau https://orcid.org/0000-0002-1372-2534
R. Miquel https://orcid.org/0000-0002-6610-4836
R. Morgan https://orcid.org/0000-0002-7016-5471
B. Nord https://orcid.org/0000-0001-6706-8972
R. L. C. Ogando https://orcid.org/0000-0003-2120-1154
F. Paz-Chinchón https://orcid.org/0000-0003-1339-2683
A. A. Plazas Malagón https://orcid.org/0000-0002-2598-0514
M. Rodriguez-Monroy https://orcid.org/0000-0001-6163-1058
A. K. Romer https://orcid.org/0000-0002-9328-879X
A. Roodman https://orcid.org/0000-0001-5326-3486
E. Sanchez https://orcid.org/0000-0002-9646-8198
M. Schubnell https://orcid.org/0000-0001-9504-2059
M. Smith https://orcid.org/0000-0002-3321-1432
E. Suchyta https://orcid.org/0000-0002-7047-9358
M. E. C. Swanson https://orcid.org/0000-0002-1488-8552
G. Tarle https://orcid.org/0000-0003-1704-0781
D. Thomas https://orcid.org/0000-0002-6325-5671
C. To https://orcid.org/0000-0001-7836-2261

References

Abbott, T. M. C., Abdalla, F. B., Allam, S., et al. 2018, ApJS, 239, 18
Agnello, A., & Spiniello, C. 2019, MNRAS, 489, 2525
Agnello, A., Treu, T., Ostrovski, F., et al. 2015, MNRAS, 454, 1260
Alard, C. 2006, arXiv:astro-ph/0606757
Allam, S. S., Tucker, D. L., Lin, H., et al. 2007, ApJL, 662, L51
Bayliss, M. B. 2012, ApJ, 744, 156
Bayliss, M. B., Hennawi, J. F., Gladders, M. D., et al. 2011, ApJS, 193, 8
Bayliss, M. B., Rigby, J. R., Sharon, K., et al. 2014, ApJ, 790, 144
Bayliss, M. B., Ruel, J., Stubbs, C. W., et al. 2016, ApJS, 227, 3
Belokurov, V., Evans, N. W., Hewett, P. C., et al. 2009, MNRAS, 392, 104
Bertin, E. 2006, in ASP Conf. Ser. 351, Astronomical Data Analysis Software and Systems XV, ed. C. Gabriel et al. (San Francisco, CA: ASP), 112
Bertin, E. 2010, SWarp: Resampling and Co-adding FITS Images Together, Astrophysics Source Code Library, ascl:1010.068
Bertin, E. 2013, PSFEx: Point Spread Function Extractor, Astrophysics Source Code Library, ascl:1301.001
Bertin, E., & Arnouts, S. 1996, A&AS, 117, 393
Bettinelli, M., Simioni, M., Aparicio, A., et al. 2016, MNRAS, 461, L67
Birrer, S., Amara, A., & Refregier, A. 2015, ApJ, 813, 102
Birrer, S., Amara, A., & Refregier, A. 2016, JCAP, 08, 020
Birrer, S., Shajib, A. J., Galan, A., et al. 2020, A&A, 643, A165
Birrer, S., & Treu, T. 2021, A&A, 649, A61
Blandford, R. D., & Narayan, R. 1992, ARA&A, 30, 311
Bleem, L. E., Bocquet, S., Stalder, B., et al. 2020, ApJS, 247, 25
Bleem, L. E., Stalder, B., de Haan, T., et al. 2015, ApJS, 216, 27
Bohlin, R. C., Gordon, K. D., & Tremblay, P.-E. 2014, PASP, 126, 711
Bolton, A. S., Burles, S., Koopmans, L. V. E., et al. 2008, ApJ, 682, 964
Bonvin, V., Courbin, F., Suyu, S. H., et al. 2017, MNRAS, 465, 4914
Buckley-Geer, E. J., Lin, H., Drabek, E. R., et al. 2011, ApJ, 742, 48
Burke, D. L., Rykoff, E. S., Allam, S., et al. 2018, AJ, 155, 41
Cabanac, R. A., Alard, C., Dantel-Fort, M., et al. 2007, A&A, 461, 813
Caminha, G. B., Grillo, C., Rosati, P., et al. 2016, A&A, 587, A80
Cañameras, R., Schuldt, S., Suyu, S. H., et al. 2020, A&A, 644, A163
Cerny, C., Sharon, K., Andrade-Santos, F., et al. 2018, ApJ, 859, 159
Chambers, K., Magnier, E., Metcalfe, N., et al. 2016, arXiv:1612.05560
Collett, T. E. 2015, ApJ, 811, 20
Collett, T. E., & Auger, M. W. 2014, MNRAS, 443, 969
Collett, T. E., Auger, M. W., Belokurov, V., Marshall, P. J., & Hall, A. C. 2012, MNRAS, 424, 2864
Collett, T. E., Buckley-Geer, E., Lin, H., et al. 2017, ApJ, 843, 148
D'Aloisio, A., & Natarajan, P. 2011, MNRAS, 411, 1628
Dark Energy Survey Collaboration, Abbott, T., Abdalla, F. B., et al. 2016, MNRAS, 460, 1270
Dark Energy Survey Collaboration, Abbott, T. M. C., Adamow, M., et al. 2021, ApJS, 255, 20
de Bom, C. R., Makler, M., Albuquerque, M. P., & Brandt, C. H. 2017, A&A, 597, A135
De Vicente, J., Sánchez, E., & Sevilla-Noarbe, I. 2016, MNRAS, 459, 3078
Diego, J. M., Schmidt, K. B., Broadhurst, T., et al. 2018, MNRAS, 473, 4279
Diehl, H. T., Allam, S. S., Annis, J., et al. 2009, ApJ, 707, 686
Diehl, H. T., Buckley-Geer, E. J., Lindgren, K. A., et al. 2017, ApJS, 232, 15
Diehl, H. T., Neilsen, E., Gruendl, R., et al. 2016, Proc. SPIE, 9910, 99101D
Diehl, H. T., Neilsen, E., Gruendl, R. A., et al. 2018, Proc. SPIE, 10704, 107040D
Diehl, H. T., Yanny, B., Tucker, D. L., et al. 2019, The Dark Energy Survey and Operations: Year 6 – The Finale, FERMILAB-TM-2720-AE, doi:10.2172/1596042
Drlica-Wagner, A., Sevilla-Noarbe, I., Rykoff, E. S., et al. 2018, ApJS, 235, 33
Ebeling, H., Qi, J., & Richard, J. 2017, MNRAS, 471, 3305
Estrada, J., Annis, J., Diehl, H. T., et al. 2007, AJ, 660, 1176
Faure, C., Kneib, J.-P., Covone, G., et al. 2008, ApJS, 176, 19
Flaugher, B., Diehl, H. T., Honscheid, K., et al. 2015, AJ, 150, 150
Fox, C., Mahler, G., Sharon, K., & Remolina González, J. D. 2021, arXiv:2104.05585
Furlanetto, C., Santiago, B. X., Makler, M., de Bom, C., & Brandt, C. H. 2013a, A&A, 549, A80
Furlanetto, C., Santiago, B. X., Makler, M., et al. 2013b, MNRAS, 432, 73
Gaia Collaboration, Brown, A. G. A., Vallenari, A., et al. 2018, A&A, 616, A1
Gates, E. 2010, Einstein's Telescope: The Hunt for Dark Matter and Dark Energy in the Universe (New York: W.W. Norton & Company)
Gavazzi, R., Marshall, P. J., Treu, T., & Sonnenfeld, A. 2014, ApJ, 785, 144
Gavazzi, R., Treu, T., Koopmans, L. V. E., et al. 2008, ApJ, 677, 1046
Gilman, D., Bovy, J., Treu, T., et al. 2021, MNRAS, 507, 2432
Grillo, C., Rosati, P., Suyu, S. H., et al. 2018, ApJ, 860, 94
Grossman, S. A., & Narayan, R. 1989, ApJ, 344, 637
Hennawi, J. F., Gladders, M. D., Oguri, M., et al. 2008, AJ, 135, 664
Hilton, M., Sifón, C., Naess, S., et al. 2021, ApJS, 253, 3
Huang, X., Storfer, C., Gu, A., et al. 2021, ApJ, 909, 27
Huang, X., Storfer, C., Ravi, V., et al. 2020, ApJ, 894, 78
Hunter, J. D. 2007, CSE, 9, 90
Jacobs, C., Collett, T., Glazebrook, K., et al. 2019a, MNRAS, 484, 5330
Jacobs, C., Collett, T., Glazebrook, K., et al. 2019b, ApJS, 243, 17
Jacobs, C., Glazebrook, K., Collett, T., More, A., & McCarthy, C. 2017, MNRAS, 471, 167
Jaelani, A. T., More, A., Oguri, M., et al. 2020, MNRAS, 495, 1291
Jauzac, M., Clément, B., Limousin, M., et al. 2014, MNRAS, 443, 1549
Joseph, R., Courbin, F., Metcalf, R. B., et al. 2014, A&A, 566, A63
Jullo, E., Natarajan, P., Kneib, J.-P., et al. 2010, Sci, 329, 924
Kessler, R., Marriner, J., Childress, M., et al. 2015, AJ, 150, 172
Kneib, J.-P., & Natarajan, P. 2011, A&ARv, 19, 47
Koopmans, L. V. E., Bolton, A., Treu, T., et al. 2009, ApJL, 703, L51
Kubik, D. 2007, PhD thesis, Northern Illinois Univ.
Kubo, J. M., Allam, S. S., Annis, J., et al. 2009, ApJL, 696, L61
Kubo, J. M., Allam, S. S., Drabek, E., et al. 2010, ApJL, 724, L137
Kubo, J. M., & Dell'Antonio, I. P. 2008, MNRAS, 385, 918
Küng, R., Saha, P., More, A., et al. 2015, MNRAS, 447, 2170
Lanusse, F., Ma, Q., Li, N., et al. 2018, MNRAS, 473, 3895
Leaf, K., & Melia, F. 2018, MNRAS, 478, 5104
Leier, D., Ferreras, I., Saha, P., et al. 2016, MNRAS, 459, 3677
Lemon, C., Auger, M. W., McMahon, R., et al. 2020, MNRAS, 494, 3491

Li, N., Gladders, M. D., Rangel, E. M., et al. 2016, ApJ, 828, 54
Li, R., Napolitano, N. R., Tortora, C., et al. 2020, ApJ, 899, 30
Lin, H., Buckley-Geer, E., Agnello, A., et al. 2017, ApJL, 838, L15
Lin, H., Buckley-Geer, E., Allam, S. S., et al. 2009, ApJ, 699, 1242
Link, R., & Pierce, M. J. 1998, ApJ, 502, 63
Lynds, R., & Petrosian, V. 1989, ApJ, 336, 1
Marshall, P. J., Verma, A., More, A., et al. 2016, MNRAS, 455, 1171
McClintock, T., Varga, T. N., Gruen, D., et al. 2019, MNRAS, 482, 1352
Meneghetti, M., Davoli, G., Bergamini, P., et al. 2020, Sci, 369, 1347
Metcalf, R. B., Meneghetti, M., Avesgtruz, C., Bellagamba, F., & de Bom, C. R. 2019, A&A, 625, A119
Mohr, J. J., Armstrong, R., Bertin, E., et al. 2012, Proc. SPIE, 8451, 84510D
More, A., Cabanac, R., More, S., et al. 2012, ApJ, 749, 38
More, A., Verma, A., Marshall, P. J., et al. 2016, MNRAS, 455, 1191
Morganson, E., Gruendl, R. A., Menanteau, F., et al. 2018, PASP, 130, 074501
Moustakas, L. A., Brownstein, J., Fadely, R., et al. 2012, AAS Meeting, 219, 146.01
Naess, S., Aiola, S., Austermann, J. E., et al. 2020, JCAP, 2020, 046
Neilsen, E. H., Jr., Annis, J. T., Diehl, H. T., et al. 2019, arXiv:1912.06254
Newman, A. B., Ellis, R. S., & Treu, T. 2015, ApJ, 814, 26
Nord, B., Buckley-Geer, E., Lin, H., et al. 2016, ApJ, 827, 51
Nord, B., Buckley-Geer, E., Lin, H., et al. 2020, MNRAS, 494, 1308
Oguri, M. 2006, MNRAS, 367, 1241
Oguri, M. 2019, RPPh, 82, 126901
Oguri, M., & Marshall, P. J. 2010, MNRAS, 405, 2579
Ostrovski, F., McMahon, R. G., Connolly, A. J., et al. 2017, MNRAS, 465, 4325
Paraficz, D., Courbin, F., Tramacere, A., et al. 2016, A&A, 592, A75
Petrillo, C. E., Tortora, C., Chatterjee, S., et al. 2017, MNRAS, 472, 1129
Petrillo, C. E., Tortora, C., Vernardos, G., et al. 2019, MNRAS, 484, 3879
Pettini, M., Christensen, L., D'Odorico, S., et al. 2010, MNRAS, 402, 2335
Plazas, A. A. 2020, Symmetry, 12, 494
Reed, S. L., McMahon, R. G., Banerji, M., et al. 2015, MNRAS, 454, 3952
Refsdal, S. 1964, MNRAS, 128, 307
Reichardt, C. L., Stalder, B., Bleem, L. E., et al. 2013, ApJ, 763, 127
Remolina González, J. D., Sharon, K., Reed, B., et al. 2020, ApJ, 902, 44
Richard, J., Patricio, V., Martinez, J., et al. 2015, MNRAS, 446, L16
Robertson, A., Smith, G. P., Massey, R., et al. 2020, MNRAS, 495, 3727
Rojas, K., Savary, E., Clément, B., et al. 2021, arXiv:2109.00014
Rozo, E., Rykoff, E. S., Koester, B. P., et al. 2009, ApJ, 703, 601
Rykoff, E. S., Rozo, E., Busha, M. T., et al. 2014, ApJ, 785, 104
Schechter, P. L., Bailyn, C. D., Barr, R., et al. 1997, ApJL, 475, L85
Seidel, G., & Bartelmann, M. 2007, A&A, 472, 341
Sevilla-Noarbe, I., Bechtol, K., Carrasco Kind, M., et al. 2021, ApJS, 254, 24
Shajib, A. J., Birrer, S., Treu, T., et al. 2020, MNRAS, 494, 6072
Sharon, K., Bayliss, M. B., Dahle, H., et al. 2020, ApJS, 247, 12
Shu, Y., Brownstein, J. R., Bolton, A. S., et al. 2017, ApJ, 851, 48
Skrutskie, M. F., Cutri, R. M., Stiening, R., et al. 2006, AJ, 131, 1163
Sonnenfeld, A., & Cautun, M. 2021, A&A, 651, A18
Sonnenfeld, A., Chan, J. H. H., Shu, Y., et al. 2018, PASJ, 70, S29
Soucail, G., Mellier, Y., Fort, B., Hammer, F., & Mathez, G. 1987, A&A, 184, L7
Stark, D. P., Auger, M., Belokurov, V., et al. 2013, MNRAS, 436, 1040
Sunyaev, R. A., & Zeldovich, Y. B. 1972, CoASP, 4, 173
Suyu, S. H., Auger, M. W., Hilbert, S., et al. 2013, ApJ, 766, 70
Suyu, S. H., Bonvin, V., Courbin, F., et al. 2017, MNRAS, 468, 2590
Talbot, M. S., Brownstein, J. R., Dawson, K. S., Kneib, J.-P., & Bautista, J. 2021, MNRAS, 502, 4617
The Dark Energy Survey Collaboration, Abbott, T., Aguena, M., et al. 2020, PhRvD, 102, 023509
Treu, T., & Ellis, R. S. 2015, ConPh, 56, 17
Walsh, D., Carswell, R. F., & Weymann, R. J. 1979, Natur, 279, 381
Wen, Z.-L., Han, J.-L., & Jiang, Y.-Y. 2011, RAA, 11, 1185
Wenger, M., Ochsenbein, F., Egret, D., et al. 2000, A&AS, 143, 9
Wiesner, M. P., Lin, H., Allam, S. S., et al. 2012, ApJ, 761, 1
Wong, K. C., Suyu, S. H., Chen, G. C. F., et al. 2020, MNRAS, 498, 1420
Wuyts, E., Barrientos, L. F., Gladders, M. D., et al. 2010, ApJ, 724, 1182
Xu, B., Postman, M., Meneghetti, M., et al. 2016, ApJ, 817, 85
Zitrin, A., Fabris, A., Merten, J., et al. 2015, ApJ, 801, 44
Zwicky, F. 1937, PhRv, 51, 290